# P-121 Detection of local structural and dynamics changes around Tyr residues in Bacteriorhodopsin corresponding to the changes of two isomers of retinal by solid-state NMR

Miyako Horigome[1], Hirohide Nishikawa[1], Izuru Kawamura[1], Satoru Tuzi[2], Takashi Okitsu[3], Akimori Wada[3], Akira Naito[1]
[1] Graduate School of Engineering, Yokohama National University
[2] Graduate School of Life Science, University of Hyogo
[3] Kobe Pharmaceutical University

Abstract
We have observed $^{13}C$ CP-MAS NMR spectrum of [1-$^{13}C$]Tyr-, [15,20-$^{13}C$]Ret-BR under temperature and pressure variation. First, we have assigned the higher and lower field peaks to the proteins corresponding to all-*trans* and 13-*cis*, 15-*syn* retinal configurations, respectively, in the dark by REDOR filter experiments. Second, conformational and dynamics changes of BR were observed and protein dynamics around Tyr was turned out to be related to temperature and pressure changes and also correlated to retinal isomerization.

Introduction
Bacteriorhodopsin (BR) has a light-driven proton pump activity triggered by photoisomerization of retinal. Retinal chromophore coexists as a mixture of all-*trans* and 13-*cis*, 15-*syn* configurations with the isomeric ratio close to 1 in the dark. Under the light irradiation, structure of retinal changes from 13-*cis*, 15-*syn* to all-*trans* and photocycle starts. During the photocycle, structure of retinal changes through intermediates (K, L, M, N, O), and consequently one proton is carried from cytoplasmic side to extracellular side. To understand the local conformational and dynamics changes of BR corresponding to the two retinal configurations in the dark and light, we have focused on the observation of protein structure around Tyr residues by means of solid-state NMR.[1)]

Materials & Methods
E1001 strain was grown in synthetic medium, where [1-$^{13}C$]Tyr-, [$^{15}N$]Pro-, [15,20-$^{13}C$]Ret-labeled BR was expressed in the purple membrane. The sample was concentrated by centrifugation and placed in 5.0 mm o.d. zirconia rotor for fast magic angle spinning (MAS) experiments. We observed $^{13}C$ CP-MAS NMR spectrum of [1-$^{13}C$]Tyr-, [15,20-$^{13}C$]Ret-labeled BR at the temperature range of 293-213 K and the spinning frequency of 4-9 kHz in the dark. We also observed photo isomerization under the light irradiated condition by means of *in-situ* photo irradiation solid state NMR.

Results & Disscussion
First, in $^{13}C$ CP-MAS NMR spectrum of [1-$^{13}C$]Tyr-BR, it was found that two major peaks applied at 176.0 (α-helix) and 174.0 (disorder state) ppm are corresponding to the proteins with two retinal configurations in the dark. Assignments of the NMR signals to the individual amino acid residue were revealed by REDOR filter experiments (Fig. 1). In $^{13}C$ CP-MAS NMR spectrum of [20-$^{13}C$]Ret-BR, it was also found that two major peaks at 13.0 and 22.0 ppm were attributed to be all-*trans* and 13-*cis*, 15-*syn* state, respectively (Fig. 2).

Second, we observed $^{13}C$ CP-MAS NMR spectrum of [1-$^{13}C$]Tyr-BR and [15,20-$^{13}C$]Ret-BR at variable temperatures. Signal intensity of [1-$^{13}C$]Tyr-BR is higher at a lower temperature and the

Keyword 1: Bacteriorhodopsin, Keyword 2: CP-MAS, Keyword 3: REDOR filter

plot of signal intensity shows a discontinuity at 260 K. It indicates that dynamical transition of protein occurred upon freezing of water and the same change was observed on the surface of purple membrane. The relative signal intensity ratio of two peaks in [20-$^{13}$C]Ret-BR at 213 K slightly increased compared with that at 293 K. However, the relative integral intensity of [20-$^{13}$C]Ret-BR didn't change largely. It was attributed to either structural change from disorder to α-helix or dynamics change in the protein around Tyr residues without change of configuration in retinal at 293-213 K.

Third, we applied pressure on BR generated by a centrifugal force in a fast MAS NMR experiments. $^{13}$C NMR signal of [1-$^{13}$C]Tyr185 corresponding to 13-*cis* state was increased under the fast MAS condition. It was noted that the isomerization from all-*trans* to 13-*cis* state was caused by the application of pressure. We will discuss the correlation between retinal and protein structure induced by pressure.

In addition, we observed $^{13}$C CP-MAS NMR difference spectrum of [1-$^{13}$C]Tyr-BR and [15,20-$^{13}$C]Ret-BR between dark and light adapted state. The signal intensity of all-*trans* state increased and that of 13-*cis* state decreased. It is suggested that configuration of retinal changed from 13-*cis,* 15-*syn* to all-*trans* state under light irradiation of the wavelength of 532 nm.

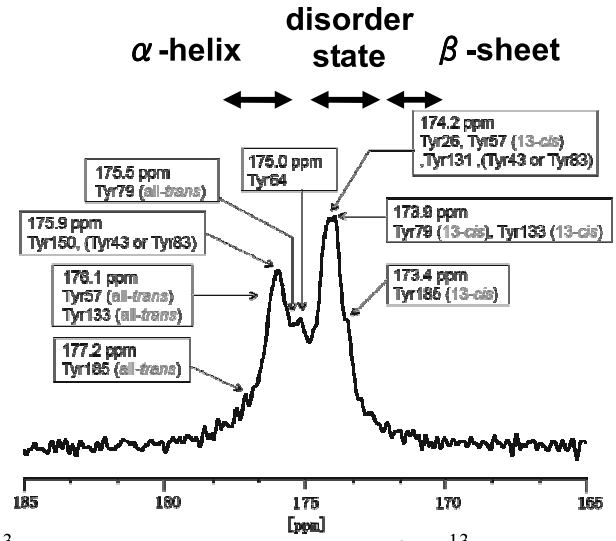


Fig. 1 $^{13}$C CP-MAS NMR spectrum of [1-$^{13}$C]Tyr-BR at 293 K
Signal assignments were performed by REDOR filter experiments. Conformation dependent chemical shift ranges are shown in the top of the spectrum.

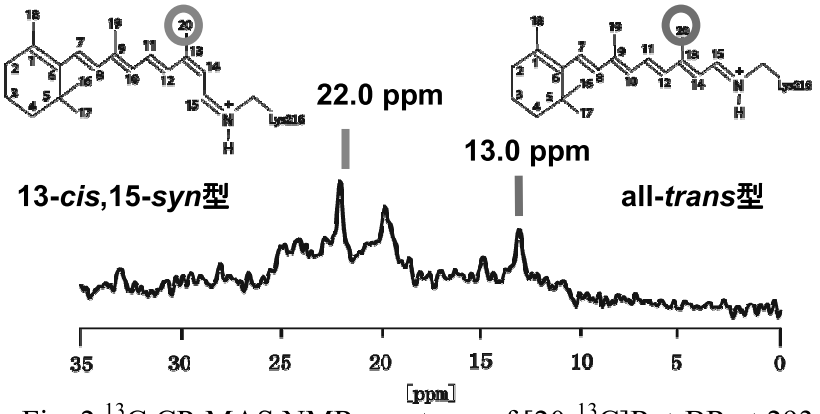


Fig. 2 $^{13}$C CP-MAS NMR spectrum of [20-$^{13}$C]Ret-BR at 293 K

Reference

1) I. Kawamura et al. *JACS* 2007, 129, 1016-1017

# P-122 Solid-state NMR analysis of $H^+$-ATP synthase subunit *c*-ring from *Thermophilic Bacillus*

Su-Jin Kang[1], Suyeon Bak[1], Yasuto Todokoro[2,3], Ikuko Yumen[2], Iku Iwasaki[2], Toshiharu Suzuki[4], Toshimichi Fujiwara[2], Masasuke Yoshida[4,5], Hideo Akutsu[1,2]

ABSTRACT

Proton-ATP synthase catalyzes ATP hydrolysis/synthesis coupled with a transmembrane $H^+$ translocation in bacterial plasma membranes. This enzyme comprises two components, water-soluble $F_1$ carrying catalytic site for the ATP synthesis/hydrolysis, and membrane-integrated $F_0$. $F_1$ is by itself a rotary motor driven by ATP hydrolysis, and $F_0$ in the membrane acts as a proton channel mediating $H^+$ translocation. The bacterial enzyme has the simplest subunit structure, $\alpha_3\beta_3\gamma\delta\varepsilon$ for $F_1$ and $ab_2c_n$ for $F_0$, respectively. The subunit $F_0$ *c*-ring of $H^+$-ATP synthase is a hydrophobic protein composed of 72 amino acid residues and plays a key role in the proton translocation caused by an electrochemical gradient across the membrane. The monomer of subunit c has a hairpin-type helix-loop-helix structure in the membrane and the number of monomers for a multimer is different on the species, which 10 subunit c from *Thermophilic Bacillus* forms a ring rotor.

Structural study of subunit *c* of $F_0$ makes it possible to explore the mechanism of proton flow through $F_0$ and its coupling with rotation. However, this work has been impeded by the unstable nature of ATP synthases, because membrane proteins generally have low expression amount and reconstitution problems in membrane mimetic environment. To overcome this difficulty, we have established an expression system for a stable membrane reconstituted ATP synthase of *Thermophilic Bacillus* PS3 ($TF_0F_1$) in *E. coli* cells. *Thermophilic Bacillus* $F_0c$-ring ($TF_0c$-ring) was highly expressed using pTR19-ASDS-cHis2R (S2H) vector in *E. coli* strain, DK8, and purified by detergent method. To assign the amino acid sequencially, we made some kinds of specifically amino acids labeled samples, using COMPAS (compensated patch assignments) method.

Furthermore, we applied solid-state NMR spectroscopy to obtain structural information of the $TF_oc$-ring reconstituted into membranes of dimyristoyl phosphatidylcholine with predeuterated acyl chains (DMPC-$d_{54}$). Solid-state NMR is one of the most powerful methods because structural analysis can be performed in a membrane environment. To assign the carbon signals, two-dimensional (2D) $^{13}C$ homonuclear correlation with DARR and 2D Cα(i+1)-Cα(i) correlation experiments were performed under magic-angle spinning (MAS). The assignment was carried out,

using fully $^{13}C$, $^{15}N$ labeled $TF_oc$ and partially $^{13}C$, $^{15}N$ labeled $TF_oc$.

---

ATP-synthase subunit c, solid-state NMR, membrane protein

P-123
Y

# The structure of retinal protein on activated state as revealed by *in-situ* photo-irradiated solid-state NMR

Yuya Tomonaga[1], Izuru Kawamura[1],Akimori Wada[2], Takashi Okitsu[2], Yuki Sudo[3], Naoki Kamo[4], Akira Naito[1]
[1]Graduate School of Engineering, Yokohama National University, Yokohama, Japan. [2]Kobe Pharmaceutical University, Kobe, Japan. [3]Nagoya University, Nagoya, Japan. [4]Matsuyama University, Matsuyama, Japan.

Retinal proteins have actions as 1) photo sensor or 2) ion transporter in microbacteria and human eyes. *p*pR (*pharaonis* phoborhodopsin) belongs to 1) photo sensor family and works to negative phototaxis in *Natronomonas pharaonis*. It is functioning through some photo-intermediates. We first developed the system of *in-situ* photo-irradiated solid-state NMR. By using this system, we have successfully detected the photo intermediate of *p*pR and revealed the structural and chemical shift changes from ground state to activated state. We will show that this system will be directly applicable to detect photo-active intermediate by *in-situ* photo irradiation.

[Introduction] *Pharaonis* phoborhodopsin (*p*pR) is a photo-receptor acting as negative phototaxis in *Natronomonas pharaonis*. *p*pR forms a 2:2 complex with its transducer protein, *p*HtrII, in the membrane. Light absorption of *p*pR initiates *trans-cis* photoisomerization of retinal chromophore followed by cyclic chmical reaction involving in several intermediates (K, L, M, and O). Among these intermediate, M intermediate is thought to be active states for signal transduction because M intermediate have long half-lifetime of 1.7 s. In fact, helix movement of *p*pR, outward tilting of the helix F, during the photocycle is suggested by various groups[1)], and it is thought to be an essential step for the activation of *p*HtrII. However no helix-tilting was observed in the crystal structure of the M-intermediate of the *p*pR/*p*HtrII complex[2)]. Thus the structural changes upon the formation of the active M-intermediate continue to be an exciting topic of discussion, though high-resolution structural studies have been a major challenge. On the other hand, solid-state NMR techniques can be applied to elucidate local structure around site-specific positions for such membrane embedded systems[3),4)]. In this study, we successfully trapped the M-intermediate using the newly developed *in-situ* photo-irradiated solid state NMR spectrometer and obtained the NMR signals from the retinal of *p*pR to gain piercing insights into the mechanism of signal transduction in *p*pR/*p*HtrII complex.

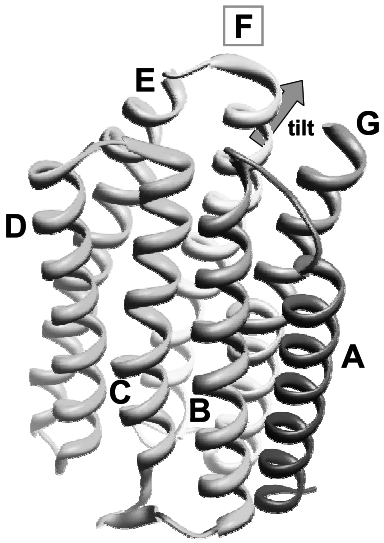

Figure 1. A crystal structure of *p*pR (PDB: 1H2S)

[Experimental] We first developed an *in-situ* photo irradiation system for solid-state NMR under the magic angle spinning condition. *In-stiu* cotinous photo-irradiation was made by an optical fiber

Retinal, NMR, membrane

from outside the magnet through a tightly sealed piece of cap made of glass rod glued to the zirconia rotor. Using this system, we could successfully irradiate green LED light (around 530 nm) of 1~100 mW to the sample in the rotor. *In-situ* photo irradiated NMR signals were acquired by means of CP-MAS and REDOR filter methods with the spinning frequency of 4kHz.

[Results and Discussion] To understand molecular mechanism of negative phototaxis, it is important to detect the conformational change of retinal as well as protein side in the photo-activated state. First, in this study, the signal of [20-$^{13}$C]Retinal in the M-state *p*pR/*p*HtrII complex split into three peaks by using in-situ photo-irradiated solid-state NMR (Fig. 2a). To observe conformational change of protein-side during photo activation, we focused on hydrogen-bond between Tyr174 and Thr204, which is the most important interaction of signal transduction in the initial process, and assigned the chemical shifts of [1-$^{13}$C]Tyr174. In the ground state of *p*pR/*p*HtrII complex, the $^{13}$C NMR signals of [1-$^{13}$C]Tyr174 appeared at 174.3 ppm and in the M-state, they appeared at 173.4, 174.0, 175.1 ppm (Fig. 2b). These results indicate that the states of individual splitting peaks are not attributed to difference of local electron density around retinal, but difference of protein-conformations. Since the peaks of Tyr and Ret in the M-state of T204A$^{ppR}$ do not show splitting, it is revealed that multi-conformations appeared only in the M-state of wt-*p*pR (Fig 2c). It is, therefore, stressed that multiple M-states is very important factor for signal transduction process.

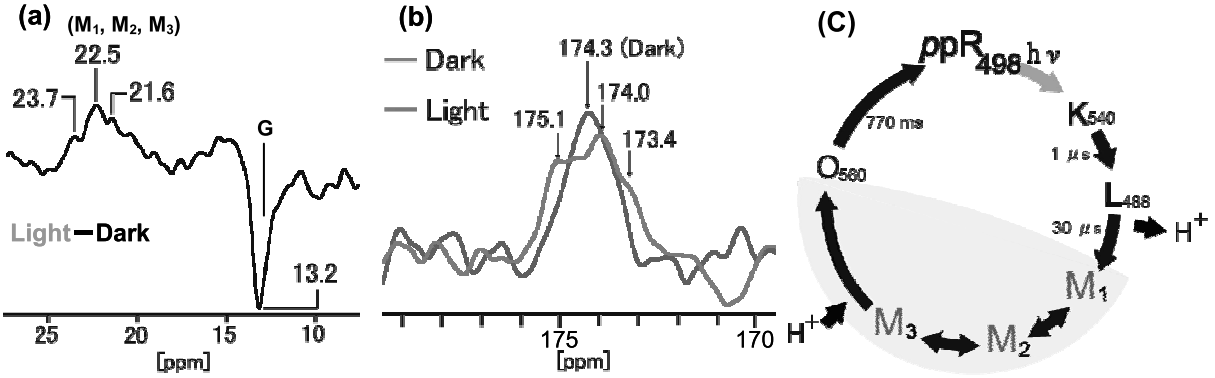


Figure 2. (a) and (b) are $^{13}$C NMR spectrum of *p*pR/*p*HtrII complex. (a) is the difference NMR spectra of $C_{20}$ between light and dark conditions. (b) is the NMR spectrum of Tyr174 in the dark and light conditions. Sample temperature is at -20℃. (c) is a new model of *p*pR-photocycle.

[Reference]


1) (a) Wegener, A.A., Chizhov, I., Engelhard, M., & Steinhoff, H.J. *J. Mol. Biol.* 2000, 301, 881-891. (b) Spudich, J. L *Mol. Microbiol.* 1998, 28, 1051-1058. (c) Yoshida, H., Sudo, Y., shimono, K., Iwamoto, M. & Kamo, N. *Biocheem. Photobiol. Sci.* 2004, 3, 537-542
2) Moukhametzianov, R., Klare, J. P., Efremov, R., Baeken, C., Goppner, A., Labahn, J., Engelhard, M., Buldt, G., & Gordeliy, V. I. *Nature* 2006, 440, 115-119
3) Kawamura, I., Yoshida, H., Ikeda, Y, Yamaguchi, S., Tuzi, S., Saito, H., Kamo, N., & Naito, A. *Photochem. Photobiol.* 2008, 84, 921-930.
4) Etzkom, M., Seidel, K., Li, L., Martell, S., Geyer, M, Engelhard, M., & Baldus, M. *Strucure* 2010, 18, 293-300

# P-124 Anisotropies of Higher Ordered Structures and Gas Diffusion of Liquid Crystalline All Aromatic Polyester with *n*-Alkyl Side Chain

Hiroaki Yoshimizu

Graduate School of Engineering, Nagoya Institute of Technology

**ABSTRACT**: The rigid-rod polyester B-Cn (n is carbon number of alkyl side chain) is one of the thermotropic liquid crystal polymers. It is formed the layered structure and filled layer space with the alkyl side chain. The layered structures of B-Cn could be easily oriented by magnetic field. In this study, these oriented and layered structures were characterized by some spectroscopic methods, and their gas transport properties were discussed. From the results, the gas sorption occurs only in the alkyl side chain layer of B-Cn, because the sorption isotherm obeys Henry's law. Diffusion coefficients of the gas in B-Cn were increased by the orientation.

## INTRODUCTION

A rigid-rod polyester with long flexible side chains (B-Cn: the number of the carbon atoms in the alkyl side chain is n) have been synthesized with 1, 4-dialkyl ester of pyromellitic acid and 4,4'-biphenol (see Fig. 1). B-Cn can form the layered structures in the crystalline and liquid crystalline phases. Fig. 2 shows the symbolized layered structure of B-Cn with flat cuboids which are corresponding to single layers of the one-dimensionally stacked main chains, and interspaces between the cuboids are side chain layers. It had been already confirmed that the gas sorption and diffusion occurred only in the side chain layers. Furthermore, it can be considered that the layered structures of B-Cn could be easily oriented by magnetic field, because of anisotropic magnetic susceptibility of benzene rings aligned to only one-direction along main chain axis in a layer. In this study, B-C14 was synthesized and used, in order to characterize the magnetically oriented layered structure of B-Cn by some NMR methods including the estimation of anisotropic diffusion of the gas molecules in B-C14.

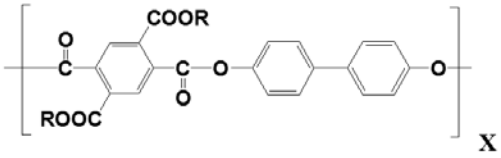


**Figure 1 Scheme of B-Cn.** R: $-(CH_2)_n-H$

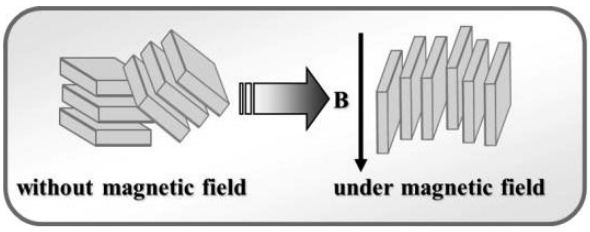


**Figure 2 Illustration of the magnetically orientation of layered structure.**

## EXPERIMENTAL

### Samples

B-C14 was prepared by converting the 1,4-dialkyl ester of pyromellitic acid to their diacid chloride followed by condensation with 4'4-biphenol. The cast film of B-C14 was annealed at desired temperature (125 ℃) under magnetic fields of 9.4 or 0 T.

### Methods

Wide-angle X-ray diffraction (WAXD) analysis was carried out with a Rigaku RAD-C X-ray diffract meter in a 2θ range of 1.5-30°. $^{13}C$ NMR spectra were recorded on a Varian Inova 400 plus spectrometer operating at 100 MHz with cross polarization technique. $CH_4$ sorption at 25 ℃ was measured by gravimetric method using a CAHN-2000 electronic micro-valance. $^{1}H$ PFGSTE

NMR of the $CH_4$ in B-C14 was measured by using a Bruker Biospin Avance DSX-300 NMR spectrometer at 300 MHz.

## RESULTS AND DISCUSSION

From a result of DSC measurement, the crystal-liquid crystal phase transition was confirmed at around 135 ℃ (heating) and 120 ℃ (cooling). B-C14 needs some fluidity for the magnetic orientation, so the annealing temperature is 125 ℃ (B-C14 is liquid crystalline state in this temperature), under magnetic field of 9.4 T. Direction of field was perpendicular to the film surface.

Fig. 3 shows WAXD profiles of the magnetic oriented B-C14 observed from edge and through views. The (100) and (001) refraction intensities were relatively strong in the profiles of through and edge views, respectively, indicate that layer structure is oriented parallel to the magnetic field applied in during sample preparation.

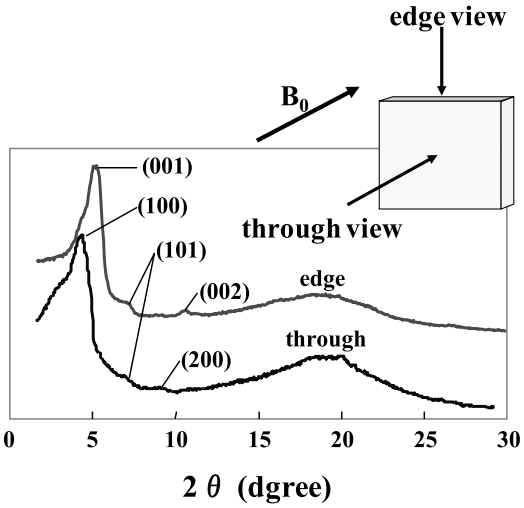


**Figure 3 WAXD profiles of B-C14 film prepared under magnetic field of 9.4T.**

Next, the solid state $^{13}C$ NMR spectra without MAS technique of magnetic oriented B-C14 were measured and some results are shown in Fig. 4. The sample setting angles in NMR SCM are indicated as an inserted picture in Fig. 4. The $^{13}C$ NMR signals assigned to aliphatic (side chain) and aromatic and carbonyl (main chain) carbons were observed at chemical shift ranges of 0-50 and 100-250 ppm, respectively. In the spectrum measured at 0° (sample setting angle between main chain axis and $B_0$ is parallel.) the peaks of main chain carbons were relatively sharp, but these became much wider like a powder pattern when the sample tilt only 30° . This finding should be interpreted from CSAs of aromatic and carbonyl carbons and cylindrical one-axis symmetry orientation of B-C14.

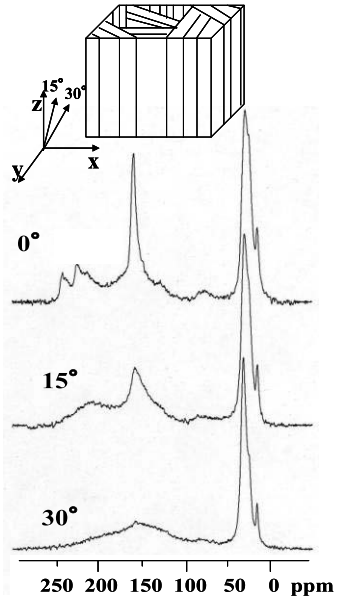


**Figure 4 $^{13}C$ CP/static NMR spectra of B-C14 at room temperature.**

Table 1 shows the result of $CH_4$ sorption measurement at 25 ℃. Solubility coefficient isn't changed by the magnetic orientation, but diffusion coefficient is larger than that of the sample prepared without magnetic field. The similar conclusions were also obtained from the self-diffusion coefficients of $CH_4$ in B-C14 samples determined by $^1H$ PFGSTE NMR.

**Table 1 Diffusion and solubility coefficients of $CH_4$ in B-C14 samples at 25 ℃ and 15.2 cmHg**

| Condition of preparation | $\bar{D}x10^8$ ($cm^2$/sec.) | $Sx10^2$ ($cm^3STP/cm^3_{polym}.cmHg$) |
|---|---|---|
| under magnetic field (9.4T) | 21.0 | 2.4 |
| without magnetic field (normal) | 7.5 | 2.4 |

Keywords: liquid crystalline polyester, magnetic orientation, gas transport properties

# P-125 Development of a solar-cell powered compact MRI system for long-term measurements of outdoor trees

Takeshi Kimura[1], Yuto Geya[1], Katsumi Kose[1,] Yasuhiko Terada[1]
Tomoyuki Haihsi[2], Kazuma Togashi[2]
Hiroshi Gemma[3,] Yoshihiko Sekozawa[3]

1. Institute of Applied Physics, University of Tsukuba
2. MRTechnology Inc
3. Agricultural and Forestry Research Center, University of Tsukuba

**Introduction**

Portable MRI systems are indispensable to measuring and monitoring of plants in outdoor environments. Last year, we developed an electrically-mobile MRI system for measurements of pear branches to clarify the mechanism of the dwarf disease of Japanese pears [1]. Using this system, we measured ADC (apparent diffusion constant) images of a pear branch for 24 hours and visualized the water function of the pear tree branch.

Our mobile MRI system can be moved more than several kilometers using several Ni-H batteries. However, because our MRI system is driven by the 100 V AC power source, this system cannot be used in the places where the AC power source is not available. This problem may be solved by using a portable electric generator. The portable electric generator, however, generates considerable electromagnetic noise detected by the NMR probe [2], and requires fuel (gasoline or LPG) refill for long-term outdoor measurements. To solve these problems, we have developed a solar-cell powered compact MRI system.

**Solar-cell powered compact MRI system**

The MRI system consists of a 0.3 T permanent magnet (80 mm gap), a gradient coil set, an RF probe, an MRI console, lead batteries, and solar-cell batteries as shown in Fig.1. The MRI console consists of an industrial PC (ADVANTEC, Tokyo, Japan), an MRI transceiver (DTRX-4, DS Technology, Asaka, Japan), a homebuilt 3CH gradient driver using power operational amplifiers (PA-12A, APEX, USA), and an RF transmitter (10 W, 10~80 MHz, Thumway, Fuji, Japan). All of the electrical units were originally powered by the 100 V AC power source, but modified to be powered by six lead batteries. We used a PC power supply with a 24 V DC input (NSP2-250-D2S, Nipron, Amagasaki, Japan). Two 84 W solar-cell panels (NT-84L5H, Sharp, Osaka, Japan) were connected to the lead batteries through a charge-up controller.

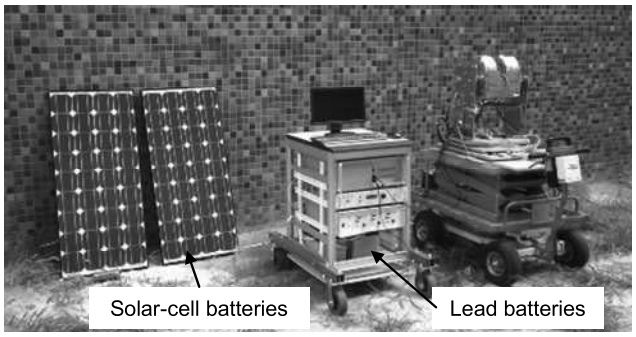


Fig. 1. Overview of the solar-cell powered compact MRI system.

MRI, solar cell plant, measurements

**Results and discussion**

Table 1 shows power consumption of the units of the MRI console measured for AC and DC power sources. This table clearly shows that about 10-50% decrease of the power consumption was achieved by the direct DC drive for the power supply.

| MRI console unit | AC power source | Battery power source |
|---|---|---|
| PC | 150W | 137W |
| NMR transceiver | 21W | 17W |
| Gradient driver | 30W | 14W |
| RF transmitter | 78W | 37W |

Table 1 Power consumption of the units of the MRI console.

Figure 2 shows cross-sectional images of a capillary phantom acquired outdoors with the DC and AC inputs to the PC power supply, respectively. The measurement parameters were TR = 200 ms, TE = 20 ms, image matrix = 256×256, slice thickness = 10 mm, FOV = $(25.6\ \text{mm})^2$. As clearly shown, the DC drive for the PC power supply generated considerable electromagnetic noise detected by the NMR RF probe. Therefore, this noise was caused by the switching circuit in the PC power supply. Although the PC power supply requires several kinds of voltage (±5V, +12V, +3.3V, etc.) and some timing control for the voltage outputs, the power should be supplied directly from the batteries.

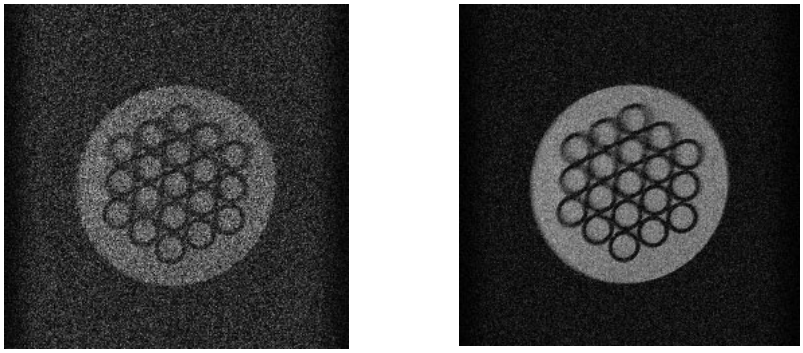

(a) (b)

Fig. 2. Cross-sectional images acquired with the solar-cell powered compact MRI system. (a) with DC input to the PC power supply. (b) with AC input to the PC power supply.

**Conclusion**

We have developed a solar-cell powered compact MRI system for outdoor long-term plant measurements. It was clarified that use of inverter circuits produced considerable electromagnetic noise and all of the electrical units should be powered directly by the batteries. We are now developing a monitoring and control system of the battery power for long-term outdoor MRI measurements.

[1] T. Kimura, Y. Geya, Y. Terada, K. Kose, T. Haishi, H. Gemma, Y. Sekozawa, ”Development of mobile magnetic resonance imaging system for outdoor tree measurements” May 17, 2011, Review of scientific instruments 82, 053704.

[2] F. Okada, S. Handa, S. Tomiha, K. Ohya, K. Kose, "Development of a portable MRI for outdoor measurements of plants", September, 2006, 6th Colloquium on Mobile Magnetic Resonance, Aachen, Germany.

# P-126

## Three Dimensional Motion Artifact Correction for Hand MR Images of Children

Daiki Tamada, Katsumi Kose
Institute of Applied Physics, University of Tsukuba

## Introduction

Motion artifacts are often observed in MR images of children if the children are not sedated. In order to reduce motion artifacts, navigator-echo methods are widely used[1]. However, it requires additional sequences, which limit optimization of the pulse sequence. In this situation, post-processing methods[2][3] are more promising, though it is challenging due to the random motion of children. Here, we propose an effective post-processing method for motion artifact correction of hand MR images of children using a minimum image entropy and registration based methods.

## Materials and Methods

Under several realistic conditions, motion during an MR scan results in phase errors in MR signals $S(k_x, k_y, k_z)$.. MR signals $S_\Delta(k_x, k_y k\_z)$ with motion errors $(\Delta x, \Delta y, \Delta z)$ can be represented as follows:

$$S_\Delta(k_x, k_y k_z) = S(k_x, k_y, k_z) e^{\left\{-2\pi i\left(\frac{k_x \Delta x}{Lx} + \frac{k_y \Delta y}{Ly} + \frac{k_z \Delta z}{Lz}\right)\right\}},$$

where $L_x$, $L_y$ and $L_z$ are FOV size along x, y and z. Therefore, motion artifacts can be corrected if phase errors can be estimated. However, it takes a long time to estimate errors completely because hand motion is generally random. Therefore, we assumed that hand motion is limited to 2D translational movements in the plane parallel to the palm of the hand in order to save computation time. This method corrects artifacts caused by translational motion during the scan. Translational motions between slices were corrected by detecting the motion using the registration based method. Translational motion between phase encoding steps in the slice in the k-space were estimated and corrected using a genetic algorithm (GA) to minimize the entropy focus criterion[3].

**Inter slice motion correction**

Phase errors between slices were calculated using the phase correlation method[4]. In this method, phase errors were estimated by determining the peak location of the normalized cross-correlation between the reference image and the displaced image. The normalized cross-correlation $P$ is given by

$$P = \mathcal{F}\left[\frac{I_r I^*}{|I_r I^*|}\right] = \mathcal{F}\left[e^{\left\{-2\pi i\left(\frac{k_x \Delta x}{Lx} + \frac{k_y \Delta y}{Ly}\right)\right\}}\right] = \delta(x + \Delta x, y + \Delta y, z + \Delta z),$$

where $I_r$, $I$ are Fourier spectra of the reference image and the displaced image, respectively. Here, both images were binarized MR images using Otsu's method[5]. We calculated cross-correlations between all slice pairs to determine the phase error of each slice acquisition.

**Motion correction for phase encoding steps in the slice (PE motion correction)**

In this case, we estimated phase errors between phase encoding steps by minimizing the image entropy[2] of MR images using a GA. The image entropy is relatively good indicator of motion artifacts. Generally, the image entropy increases as phase errors are getting larger. A fitness function of the GA was defined as follows:

$$fitness = -\sum_i \frac{G_i}{G_{max}} \log \frac{G_i}{G_{max}}, \qquad G_{max} = \sqrt{\sum_i (G_i)^2},$$

MRI, motion artifact, genetic algorithm

where $G_i$ is the signal intensity of the MR image convolved with a _rst derivative operator. In this method, we corrected individual phase errors for each read-out line from the scan center (zero phase encode gradient) toward the end of the scan.

## Results and Discussion

Phantom and volunteer studies were performed to demonstrate our method. A phantom (diameter=60 mm) was measured using a 0.2 T MRI system with a 2D spin echo sequence (TE/TR=20/100 ms, matrix size=$128^2$). The phantom was moved during the scan. Therefore, the motion artifact was observed in the phantom image as shown in Fig. 1(a). Figure 1(b) shows an MR image with PE motion correction. Ghosting and blurring due to motion were nearly removed via minimizing the image entropy (Fig. 1(c)).

The hand MR image (Fig. 2(a)) of a child (4 years old) was measured using a 0.3 T MRI system with a 3D gradient echo sequence (TE/TR=10/40 ms, matrix size=512×128×32). Anatomic structures of the image were not clear due to motion during the scan. Figure 2(b) shows the MR image after slice and PE motion correction. Motion artifacts were also removed in this case.

## Conclusion

Our method was demonstrated to correct motion artifacts for the phantom and hand MR images. Phase errors induced by motion were estimated using the minimum image entropy method and phase correlation method. As a result, image quality of MR images was improved. Using our method, scanning time can be saved because it is not necessary to rescan the children. Therefore, we concluded our method is useful for MR imaging of children.

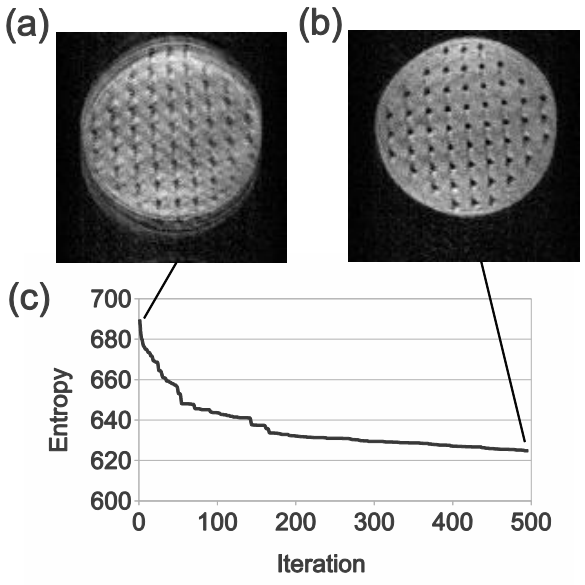


Figure 1: (a) Phantom MR image acquired using a SE sequence(TE/TR=20/100 ms, matrix size = $128^2$). (b) MR image with PE motion correction. (c) Image entropy plotted as iterations in a GA.

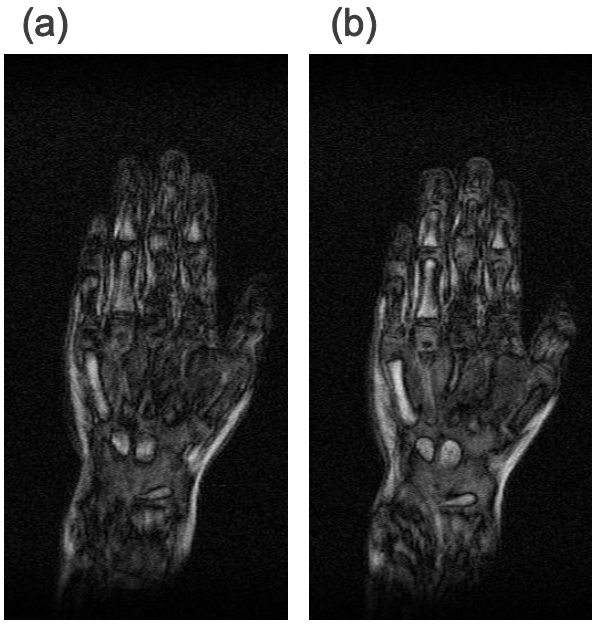


Figure 2: (a) MR image of left hand of a child acquired using a gradient echo sequence (TE/TR=10/40 ms, matrix size=512×128×32). (b) MR image with slice and PE motion correction.

## References

[1] Z.W.Fu, Y.Wang and R.C.Grimm Magn Reson Med, 35, 763(1995).
[2] M.H.Buonocore and L.Gao, Magn Reson Med, 38, 89(1997).
[3] D.Atkinson and D.Hill, IEEE Trans. Med. Imaging, 16, 903(1997).
[4] L.G.Brown, ACM Com- put. Surv. (CSUR), 24, 325(1992).
[5] N.Otsu, IEEE Trans. Sys., Man., Cyber, 9, 62(1972).

# P-127 Quantitative multinuclear MRI

Ryo Yamada[1], Naoki Ichijo[1] K. Takegoshi[1] and Kazuyuki Takeda[1]
[1]Division of Chemistry, Graduate School of Science, Kyoto University

Abstract
In order to perform MRI of $^{1}H$, $^{19}F$, $^{31}P$, and $^{23}Na$ spins, we developed an experimental system employing a cryogen-free, field variable superconducting magnet. Static-field variation allows access to various spin species at a common Larmor frequency. Since the efficiency of rf signal transmission are the same, the relative amount of spins can be obtained in a straightforward manner. The quantitative multinuclear NMR in combination with imaging experiments can give fruitful information in both material sciences and *in vivo* studies.

Studies on multinuclear MRI reported so far[1][2][3] used a fixed magnetic field. However, quantitative evaluation of the relative amount of the individual nuclear spin species is challenging. This is because the efficiencies of nuclear induction and signal transmission change with the frequency.

In this work, we explore the feasibility of multinuclear MRI using a fixed frequency and variable static fields. In this case, the relative signal intensity is determined solely by the macroscopic nuclear magnetization. In thermal equilibrium at temperature T, the magnetization $M_i$ of the *i*th spin species is given by the Curie's Law as

$$M_i = \frac{N_i \gamma_i^2 \hbar^2 I_i (I_i+1) B_{0i}}{3k_B T} \quad (1)$$

Here, $N_i$ is the number of nuclear spins, $\gamma_i$ is the gyromagnetic ratio, and $I_i$ is the spin quantum number.

Since the frequency $\omega_0$ is fixed, the external field $B_{0i}$ has to be adjusted according to

$$B_{0i} = \frac{\omega_0}{|\gamma_i|} \quad (2)$$

By inserting Eq.(2) into Eq.(1), we obtain

$$N_i = C \frac{M_i}{\gamma_i I_i (I_i+1)} \quad (3)$$

where C is a constant. It follows that the relative number of the *i*th spin is obtained from the measured magnetization. A new approach to NMR elemental analysis based on this idea is presented in a separate poster[4].

keywords:MRI, multinuclear, quantification

Here, we aim at combining MRI with NMR element analysis toward quantitative multinuclear MRI. For this purpose, we developed an experimental system, which consists of a field-variable superconducting magnet (Cryogenic Ltd.), a home-built probe equipped with field-gradient coils, and a home-built spectrometer[5]. In this system, the magnetic field can be varied up to 7 T. Our target nuclei are $^{1}H$, $^{19}F$, $^{23}Na$, and $^{31}P$. Among them, $^{23}Na$ has the lowest gyromagnetic ratio of 11.3 MHz/T. Accordingly, we chose the constant resonance frequency of 81 MHz, and have started the project of frequency-fixed, quantitative multinuclear MRI.

References

[1]Koptyug,I. V. et al.(2007),Applied Magnetic Resonance,**32**,321-331.
[2]Wu,Y. et al.(1999),Proceedings of the National Academy of Sciences,**96**,1574 -1578.
[3]Hankiewicz,J. et al.(2003),Applied Magnetic Resonance,**24**,393-400.
[4]Ichijo,N., Takeda,K., and Takegoshi,K. poster session
[5]Takeda K.(2008),Journal of Magnetic Resonance,**192**,218-229.

# P-128 MRI Study of vascular grafts based on silk fibroin fibers

Shigeki Kuroki[1], Koji Yazawa[2], Kotaro Isobe[2], Tetsuo Asakura[2]
[1]Department of Organic and Polymeric Materials, Tokyo Institute of Technology, [2] Department of Biotechnology, Tokyo University of Agriculture and Technology

**ABSTRACT**

Computer-controlled double-raschel knitted silk fiber tubes coated with silk fibroin or polyurethane sponges were prepared. The $^{1}H$ spin density, $^{1}H$ $T_2$ and diffusion coefficient of water in the coating layers was observed using MR Imaging. The amount and mobility of water molecules in the coating layer change largely between two kinds of the coating materials.

**INTRODUCTION**

In the field of surgical revascularization, the need for functional small-diameter (less than 6 mm in diameter) vascular grafts is increasing. Several synthetic biomaterials have been tested for this purpose, but in many cases they cause easily thrombosis. We prepared small-diameter (1.5 mm) vascular graft of silk fibroin fibers by braiding and winding, and implanted the silk graft to rat. Excellent long-term patency together with remodeling of the graft was obtained. Thus, it can be proved that silk is a promising material to small-diameter vascular graft. [1-3] Recently, there are several reports on the close relationship between the state and mobility of water molecules on the graft materials, and the thrombosis of the graft.

In this work, the spatial distribution of $^{1}H$ density, $T_2$ and diffusion coefficient of water molecules in the coating layer of the grafts was observed using MR imaging. The state and mobility of water molecules will be discussed in relation with the thrombosis of the grafts.

**EXPERIMENTAL**

*Preparation of the vascular graft from silk fibers:* Computer-controlled double-raschel knitted silk fiber tubes with different diameters were prepared because of high strength of the double-raschel knitted silk graft and protection of loosing from the end of the graft in the implantation process. In order to protect leakage of the blood and giving further strength and elasticity, the coating of the grafts is required.

Two types of the coating materials were used. Namely, the adhesive character of endothelial cells, HUVEC (black dots) on the films was quite different between silk and polyurethane as shown in Fig.1. High adhesive character was observed for silk fibroin, but essentially no cell-adhesive character for polyurethane. Therefore the inside of the silk graft was coated by silk fibroin sponge, but the outside was coated by polyurethane or silk fibroin sponges. It is expected that the amount and mobility of water molecules in the coating layer change largely between two kinds of the coating materials. The former is noted as VG-SS and the latter VG-US. The thickness of both grafts after coating was 0.5 mm.

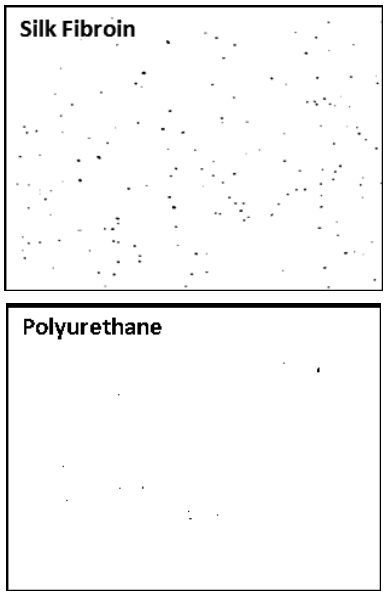


Fig.1 The cell adhesive experiment with silk fibroin and polyurethane films.

*MRI measurement:* $^{1}H$ MR imaging measurements were carried out in a Bruker Biospin Avance DSX 300 NMR spectrometer operating at 300 MHz with an imaging system at 300K. For the acquisition and processing of NMR data, the ParaVision program supplied by Bruker Biospin was used. Two types of experiment were performed.

Keyword; vascular grafts, silk fibrin, MR Imaging

One is the spin echo method for obtaining $^1$H spin density and $^1$H $T_2$. Another is field gradient spin echo method for obtaining the diffusion coefficient of water molecules. The vascular grafts were set in an NMR tube with a diameter of 5 mm and filled by pure water.

## RESULTS AND DISCUSSION

The $^1$H spin density map and $T_2$ map were constructed by using the spin-echo MR images with echo time of 8.6, 17.2, 25.8, 34.4, 43.0, 51.6, 60.2 and 68.8 ms. Fig.2 shows $^1$H spin density map of VG-SS (a) and VG-US (b), and $^1$H $T_2$ map of VG-SS (c) and VG-US (d), respectively. It is noted that the $^1$H spin density in the layer of VG-SS is higher than that of VG-US. It means that the amount of water in the layer of VG-SS is larger than that of VG-US. From SEM images, it was shown that the outer coating material also exists in the layer of grafts (Data not shown). Thus, the obtained data are reasonable because silk fibroin is more hydrophilic than polyurethane.

The $^1$H $T_2$ of water molecules in the layer of VG-SS is 15-20 ms and that of VG-US is 25-30 ms. It means that the mobility of water in VG-US is higher than that of VG-SS. The mobility of water molecules decrease remarkably because of strong binding interaction between silk fibroin and water molecules, but there is no strong interaction between hydrophobic polyurethane and water molecules. Actually, the mobility of water molecules in the layer of VG-US is almost the same as that of bulk water. These results indicate that the amount and mobility of water molecules in the coating layer change largely by the nature of the materials. The difference in the thrombosis of the graft is now studying.

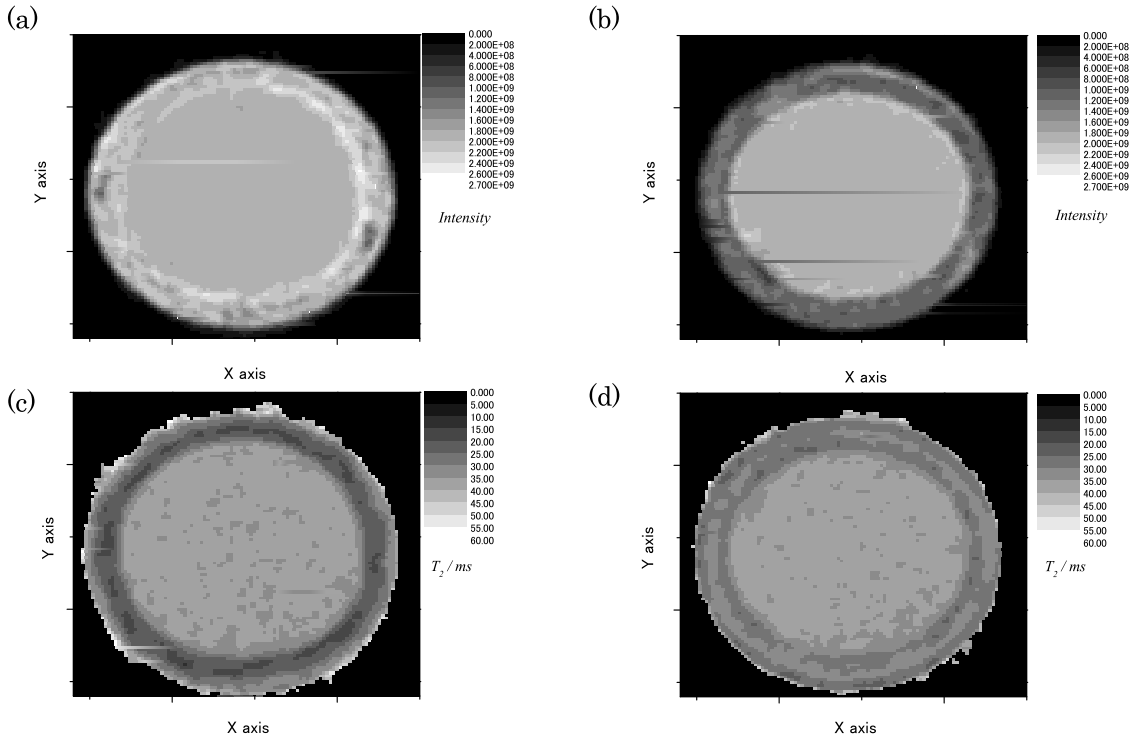


Fig.2 $^1$H spin density map of VG-SS (a) and VG-US (b), and $^1$H $T_2$ map of VG-SS (c) and VG-US (d), respectively.


## ACKNOWLEDGEMENT

TA and SK acknowledge the financial supports from Grant-in-Aid for Scientific Research from Ministry of Education, Science, Culture and Supports of Japan (TA; 23245045) and (SK and TA; 21550112), and TA also acknowledge Agri-Health Translational Research Project from the Ministry of Agriculture, Forestry and Fisheries, JAPAN.


## REFERENCES


1.S. Enomoto, T. Asakura et al., JVS., **51**,155-164 (2010).
2.Y. Nakazawa, T. Asakura, et al., *J.Biomater. Sci.,***22**,195-206 (2010).
3.T.Yagi, T.Asakura et al., *JAO.*, **14**,89-99 (2011).

# P-129 Hyperpolarized $^{129}$Xe magnetic resonance imaging in rat lung

Mineyuki Hattori[1], Tomokazu Numano[1,2], Koji Hyodo[1], Kazuhiro Homma[1]
[1]National Institute of Advanced Industrial Science and Technology and
[2]Tokyo Metropolitan University

ABSTRACT: The hyperpolarization (HP) technique can increase the signal sensitivity of nuclear magnetic resonance (NMR) by a factor of 10,000 for $^{3}$He and $^{129}$Xe, and thus it enables the instantaneous imaging of cavity gases [1, 2]. This technology is expected to be applied to the development of medical equipment that enables the instantaneous evaluation of lung functions and the early diagnosis and prevention of cerebral infarction based on high-accuracy and high-speed imaging of the blood flow in the brain [3]. We have developed a practical device that uses a batch method to provide a continuous supply of HP xenon gas with a sufficient rate of polarization for practical biomedical MRI experiments. The possibility of producing HP xenon gas on demand had made the use of MRI equipment much easier [4]. For the biomedical application of HP xenon gas, we have installed a generator adjacent to a horizontal 2 T MRI system. In this paper, we report our experiment on the rapid imaging of a rat lung using HP $^{129}$Xe.

Methods: All MRI experiments were performed using the 2 T MRI system (Bruker Biospec with Oxford 2 T/31 cm SCM). We developed a two-channel combined coil system, in which one channel was an 8-element birdcage coil, which was tuned to the $^{129}$Xe frequency (~23.56 MHz) and had an inside diameter of 70 mm, and the other channel was an “8”-character-shaped saddle coil, which was tuned to the $^{1}$H frequency (~85.16 MHz) (Takashima Seisakusho). The HP xenon gas was generated by a Toyoko Kagaku HPXE2105S polarizer [4]. The stray field of the horizontal SCM was used for optical pumping. The optical pumping cell was heated to 140 $^{o}$C in a magnetic field of approximately 12 mT and irradiated with circularly polarized light with a wavelength of 794.7 ± 1.5 nm using a 40 W semiconductor laser (QPC Lasers : 4007-0000) and a quarter-wave plate (CVI : QWPO-795-08-4-R10). After 30 min, the HP xenon gas was produced with a polarization rate of 2-3% for $^{129}$Xe from a gas mixture of Xe (98%) and $N_2$ (2%). The HP xenon gas was transported to a 60 ML plastic syringe. In vivo experiments were conducted on anesthetized Crj:Wistar rats (n＝4, ~300 g). Each animal was anesthetized with an intraperitoneal injection of ketamin (100 mg/ kg body weight), xylazine (10mg/kg body weight) and atropine (0.05mg/kg body weight). An endotracheal tube was inserted into the trachea and a thinner tube (silica capillary tube, GL Science) was also inserted into the tracheal tube to ensure inhalation of the polarized gas by the rat's lung. The anesthesia was maintained using isoflurane (1%) mixed with 0.3 l/min oxygen and 0.7 l/min nitrous oxide gas using a respirator (Shinano Seisakusho : SN-480). Before starting MRI acquisition, the respirator was stopped and 60 cm$^3$ of the polarized gas was insufflated manually (2 cm$^3$/s after rapid purging of 10 cm$^3$) by means of spontaneous respiration through the endotracheal tube inserted by tracheotomy.

hyperpolarization, xenon, lung

Results: MRI acquisition experiments applying FID acquisition-type EPI (EPI-FID) and spin echo acquisition-type EPI (EPI-SE) sequences were completed with 1 s time resolution using the coil. In our experiment, the quality of the image obtained using EPI-FID (TE=8.9 ms, NEX=1, 32 X 32) was almost the same as that using EPI-SE (TE=20.9 ms, NEX=1, 32 X 32) for the Xe in the rat lung. Figure 1 shows the EPI-FID and EPI-SE images and $^{1}$H scout image (FLASH, TE=4.3ms, TR=25ms, FA=30$^{o}$, 256 X 128, FOV=17.4cm) obtained in the experiments.

Figure 1
HP $^{129}$Xe image using EPI-SE, HP $^{129}$Xe image using EPI-FID, $^{1}$H image using GE (scout)

Conclusion: The time resolution of the MRI acquisition of the HP xenon was shortened to about 50 ms for a single-shot EPI sequence. Faster acquisition sequences are an essential technology for the high-accuracy and high-speed imaging of the gas dynamics in the lung or the blood flow in the brain. The results of this study should facilitate work on MRI to shorten measuring times, produce more diverse information, and increase accuracy.

References:
[1] W. Happer, E. Miron, S. Schaefer, D. Schreiber, W. A. van Wijngaarden, X. Zeng, Phys. Rev. A**29**, 3092 (1984).
[2] M. S. Albert, G. D. Cates, B. Driehuys, W. Happer, B. Saam, C. S. Springer Jr., A. Wishnia, Nature **370**, 199-201 (1994).
[3] S. D. Swanson, M. S. Rosen, B. W. Agranoff, K. P. Coulter, R. C. Welsh, T. E. Chupp, Magn. Reson. Med., **38**, 695-698 (1997).
[4] (a) M. Hattori, Proc. ISMRM, **15**, 1264 (2007). (b) N. Ohtake, M. Murayama, T. Hiraga, M. Hattori, K. Homma, Japanese Patent 2003-4304, January 10, 2003.

# P-130 Metabonomics sequences as a tool to visualize the complex metabolic dynamics of superorganisms

Yasuhiro Date[1,2], Tomohiro Iikura[2] and Jun Kikuchi[1,2,3,4]

[1]RIKEN Plant Science Center
[2]Graduate School of Nanobiosciences, Yokohama City University
[3]Biomass Engineering Program, RIKEN Research Cluster for Innovation
[4]Graduate School of Bioagricultural Sciences, Nagoya University

Metabolic dynamics in 'superorganisms' (i.e. environmental ecosystems) are created by complex, diverse, and extensive interactions and competitions in microbial community and its environments. Therefore, the development of the visualization method like a 'birds-eye view' is important to characterize the entire sequential metabolic process in the environmental ecosystems. In this study, we developed an approach for visualization of metabonomics sequences in various environmental ecosystems to characterize the comprehensive metabolic dynamics by combination of microbial community profiles and NMR-based metabonomics profiles. By evaluating their time-dependent variation, we found that microbial community profiles and metabolite production processes were characteristically affected by the feedings of different substrates. This combinatorial approach to variation in microbial communities and metabolic profiles was used successfully to visualize metabonomics sequences in anaerobic fermentation ecosystem and host-microbial symbiotic ecosystem. Thus, this approach provides a powerful tool for visualizing and evaluating metabonomics sequences in various environmental ecosystems.

**[Introduction]**

Highly complex animals such as humans can be considered superorganisms with an internal ecosystem of diverse symbiotic microbiota and parasites that have interactive metabolic processes.[1] In addition, entire metabolic processes in environmental ecosystems such as anaerobic fermentation generating in various environments are caused as the results of interactions between microbial and environmental systems. These complex biological systems are therefore behaved like a superorganism. Thus, the various environments including the broad ranges from animal-microbial symbiotic systems to environmental ecosystems must be visualized as an entire ecosystem where chemical interactions occur at multiple organizational levels with cross-talk between microbial and their environmental systems.

Metabolic dynamics in the superorganisms are created by complex, diverse, and extensive interactions and competitions in microbial community and its environments. Due to the complexity of sequential metabonomics in the superorganisms, conventional bottom-up approaches to identify the metabolic dynamics in an entire ecosystem may be inadequate to visualize the comprehensive metabolic dynamics and networks within a microbial community. Thus, it is important to develop visualization methods that provide a bird's-eye view to characterize the entire sequential metabolic process in various environmental ecosystems by applying a NMR-based metabonomics approach with multivariate statistical analyses.

Keywords: metabonomics sequences/ visualization method/ microbial ecosystems

Within the field of metabonomics, measurement of system responses over time is usually important to obtain a complete picture of metabolic dynamics after or during the application of some input to an environment, such as a drug or food in human intestines, because the variations in each metabolite have intrinsic behaviors.[1,2] Thus, time-dependent variations and timed responses should be considered and applied in the development of a visualization method when evaluating and characterizing metabolic dynamics in microbial ecosystems.

In this study, we used a top-down systems biology approach and multivariate statistical analyses to develop an approach for the visualization of metabonomics sequences in an anaerobic fermentation ecosystem and a host-microbial symbiotic ecosystem to characterize the comprehensive metabolic dynamics in microbial communities. To this end, we visualized and compared the degradation processes of glucose, starch, and cellulose in an anaerobic fermentation ecosystem and viscous substrates in Japanese bunching onions in an intestinal symbiotic ecosystem to evaluate the entire metabolic dynamics of the microbial ecosystems using a combinatorial approach of microbial community profiles and metabolic profiles (Fig. 1).

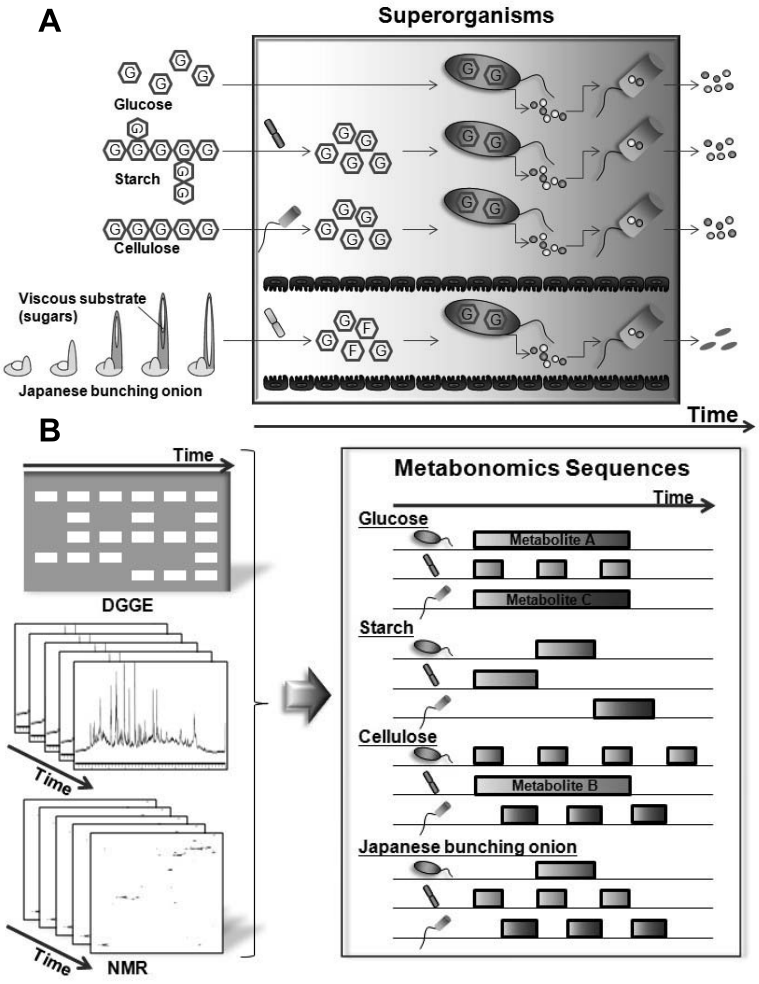


**Figure 1**. Schematic overview of the visualization method for metabonomics sequences in superorganisms. (**A**) Schematic view of the degradation processes of glucose, starch, cellulose, and viscous substrate in Japanese bunching onion in superorganisms. (**B**) The experimental flow for evaluating metabonomics sequences. Time-dependent variations in microbial community and metabolic profiles were evaluated using DGGE fingerprinting and NMR spectroscopy. Correlated datasets were visualized and compared as metabonomics sequences in each system.

**[Materials and Methods]**

A high-temperature methane fermentation sludge used for residual food processing was prepared for evaluation of anaerobic fermentation ecosystems. Sludge was inoculated in each STR with 2.3 g of D-glucose, 2.1 g of cornstarch, or 2.1 g of α-cellulose as a substrate at a constant temperature of 55°C under anaerobic conditions. Pellets from collected samples (1 mL) were used for microbial community analysis.

In animal experiments for evaluation of intestinal symbiotic ecosystem, male 10-week-old BALB/cA mice (CLEA Japan, Inc., Japan) were housed at 23 to 25°C and 50 to 60% relative humidity with a 12 h light-dark cycle. The experimental diet consisted of 5% viscous substrates of Japanese bunching onion mixed with CLEA Rodent Diet CA-1 (CLEA Japan, Inc., Japan). The mice were fed the

experimental diet alternating with CA-1 diet biweekly for four weeks. Fecal pellets and urinary samples were collected daily from each mouse.

To evaluate the microbial community profiles, DNA extraction, PCR amplification, denaturing gradient gel electrophoresis (DGGE), and phylogenetic analysis was performed as described previously.[3] To evaluate the metabolic profiles, supernatants of collected samples were suspended with 10% (v/v) deuterium oxide ($D_2O$) and 1 mM sodium 2,2-dimethyl-2-silapentane-5-sulfonate (DSS) as an internal standard. The methods for the NMR measurements of $^1$H-NMR spectra and two-dimensional (2D) $^1$H-$^{13}$C heteronuclear single quantum coherence (HSQC) and total correlation spectroscopy (TOCSY) were described previously.[3–9] NMR spectra were processed using NMRPipe software[10, 11] and were assigned using the SpinAssign program at the PRIMe website.[12–14]

For principle components analysis (PCA) and correlation analysis of DGGE and $^1$H-NMR spectra, signal intensities and band positions in each lane of DGGE images were divided into a spectrum consisting of 100 variables. $^1$H-NMR data were reduced by subdividing spectra into sequential 0.04 ppm-designated regions between $^1$H chemical shifts of 0.0 to 9.0. PCA was run in the 'R' software. Data were visualized in the form of PC score plots and loading plots. Each coordinate on the score plot represented an individual sample and each coordinate on the loading plot represented DGGE bands related to bacteria and $^1$H-NMR spectral data points related to metabolites. A 2D correlation map was calculated as a symmetric matrix using Pearson's product-moment correlation coefficient in which an element at position ($i$, $j$) is defined as a correlation coefficient between the $i^{th}$ and $j^{th}$ positions in a set of $^1$H-NMR spectra and DGGE gel bands of the identified major bacteria. A more positive (negative) coefficient indicates the existence of a positive (negative) correlation between the $i^{th}$ and $j^{th}$ peaks or bands.

**[Results and Discussion]**

To identify and compare the metabolic dynamics by microbial community in each superoganism, microbial community profiles and metabolic profiles in each system were analyzed using DGGE fingerprints and NMR-based metabonomics approaches, respectively. The intensities of the major bands detected in DGGE analysis and $^1$H-NMR chemical shift data were digitized and statistically compared to evaluate the variability of the microbial community profiles and metabolic profiles in each superoganism. The results of PCA for DGGE fingerprinting data and $^1$H-NMR chemical shift data revealed that microbial community profiles and metabolite production processes were characteristically affected by the feedings of different substrates.

To link the variability in microbial community profiles and metabolic profiles in each superoganism, we performed microbial-metabolic correlation analyses based on DGGE fingerprints and $^1$H-NMR chemical shift data using Pearson's product-moment correlation coefficient. This DGGE-NMR correlation analysis identified the relationship between microbial community and metabolites. For example, bands 2, 3, 4, 8, and 9 in anaerobic fermentation ecosystem were negatively correlated with glucose (Fig. 2). This indicates the possibility that glucose was used by bacteria related to bands 2, 3, 4, 8, and 9. Additionally, band 8 was positively correlated with propionic acid and butyric acid. This indicates the possibility that propionic acid and butyric acid were produced by bacteria related to band 8. Taken together, the microbial variability and metabolic dynamics of the microbial community were found to be closely linked to each other.

Interestingly, 2D correlation maps indicated differences in the roles and relationships between metabolites and bacteria in the substrate degradation processes in anaerobic fermentation

ecosystems. The role played by individual bacteria in the metabolic dynamics of the microbial community in anaerobic fermentation ecosystems differed, as summarized in Figure 2. Thus, using the approach described here, it was possible to visualize characteristic metabonomics sequences in superoganisms.

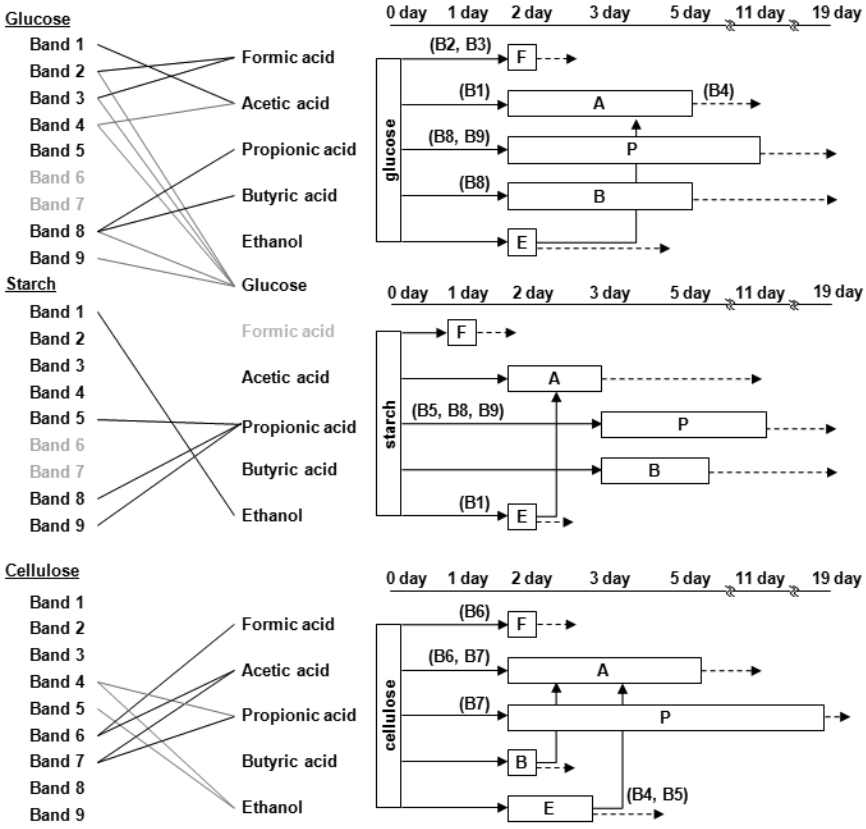


**Figure 2**. Visualization of metabonomics sequences processed by microbial community in anaerobic fermentation ecosystems. Associations between specific metabolites and each band detected in the DGGE analysis are shown as the correlation lines indicated by black (positive) or gray (negative). Solid lines in the right panels indicate the production of metabolites, and broken lines in the right panels indicate the utilization of metabolites by the microbial community. Each box in the right panels was defined in ranges from a top (or near top) peak after marked elevation of each metabolite to below half the amount of the top peak, calculated according to the quantitative data. Abbreviations: B1 to B9, bands 1 to 9, detected in DGGE analysis; A, acetic acid; B, butyric acid; E, ethanol; F, formic acid; P, propionic acid.

This study focused on the degradation processes of glucose, starch, cellulose, and viscous substrate in Japanese bunching onions in superoganisms, and visualized and compared metabolic dynamics in individual microbial communities using a sequential metabonomics approach based on DGGE-NMR correlation analysis. This approach may be a useful tool for visualizing and evaluating the metabonomics sequences of biomass degradation processes in environmental ecosystems. By applying our approach to other complex and diverse microbial ecosystems, including various environments such as oceans, soils, and symbiotic ecosystems, we should be able to decipher and readily compare comprehensive metabonomics sequences in a variety of microbial ecosystems.

## [References]


(1) Nicholson, J. K. *et al*., *Nat. Biotechnol.* **2004,** *22*, 1268-1274., (2) Nicholson, J. K. *et al*., *Nat. Rev. Drug Discovery* **2002**, *1*, 153-161., (3) Date, Y. *et al*., *J. Biosci. Bioeng.* **2010,** *110*, 87-93., (4) Fukuda, S. *et al*., *PLoS ONE* **2009,** *4*, e4893., (5) Kikuchi, J. and Hirayama, T., *Methods Mol. Biol.* **2007,** *358*, 273-286., (6) Nakanishi, Y. *et al*., *J. Proteome Res.* **2011,** *10*, 824-836., (7) Sekiyama, Y. *et al*., *Anal. Chem.* **2010,** *82*, 1643-1652., (8) Sekiyama, Y. *et al*., *Anal. Chem.* **2011,** *83*, 719-726., (9) Sekiyama, Y. and Kikuchi, J., *Phytochemistry* **2007,** *68*, 2320-2329., (10) Delaglio, F. *et al*., *J. Biomol. NMR* **1995,** *6*, 277-293., (11) Kikuchi, J. *et al*., *Plant Cell Physiol.* **2004,** *45*, 1099-1104., (12) Akiyama, K. *et al*., *In Silico Biol.* **2008**, *8*, 339-45., (13) Chikayama, E. *et al*., *Anal. Chem.* **2010,** *82*, 1653-1658., (14) Chikayama, E. *et al*., *PLoS ONE* **2008,** *3*, e3805.

# P-131 Contribution of chemical exchange to $R_2$ in agarose and gelatin gels

Nobuhiro Takaya[1], Hidehiro Watanabe[1] and Fumiyuki Mitsumori[1]
[1] National Institute for Environmental Studies. Tsukuba, JAPAN

Introduction

$T_2$ is one of the most important contrast sources for disease diagnosis and brain functional mapping in human brain. We found that the apparent transverse relaxation rate ($R_2^{\dagger}$) of tissue water in human brain was explained with a linear combination of contributions from the ferritin iron and the macromolecular mass fraction defined as 1-water fraction [1]. To understand relaxation mechanisms underlying we have examined the field dependence of $R_2$ of the water molecule in a model system of agarose and gelatin. The field dependence was different in two gel systems [2]. In the present study, to investigate the cause of the difference, $R_2$ analysis on those gel samples at various fields was performed using the chemical exchange model.

Materials and Methods

Gelatin (100bloom) and agarose powder were dissolved in 100mM NaCl solution at 60°C. Final concentrations were 10% (pH4) and 1% (pH7) respectively. 4.7T (Varian), 11.7T (JEOL), and 18.8T (JEOL) MRI or NMR spectrometers were used for $T_2$ measurements. $T_2$ was measured using a Carr-Purcell-Meiboom-Gill (CPMG) method. The 90-180° pulse spacing ($\tau$ = (1/2) echo spacing) was varied between 0.125ms and 8ms. Variable numbers of echo were collected dependent on the sample $T_2$ values. Intensity of water signal in the echo train was fitted with a single exponential curve to get a $T_2$ value.

Result and Discussions

In gelatin gel, a linear dependence of $T_2$ on the field was observed. In contrast, Relaxation measurements for agarose gel didn't show dependence of $T_2$ with the magnetic field ($B_0$). Figure1 shows the variation in $R_2$ as a function of inter-echo time in gelatin gel. $R_2$ values for gelatin gel decreased markedly with decreasing $\tau$. While the effect of $\tau$ was observed at all fields for gelatin gel, only a small effect was found at 18.8T for agarose gel (Fig.2). This behavior of $R_2$ as a function of $\tau$ may be explained by exchange of protons between water and exchangeable protons in gels. The relaxation rate is given by the Luz - Meiboom relation [3] as:

$$R_2 = O + F_2(\delta\omega)^2 / k_{EX} \left[1 - 1/k_{EX}\tau \tanh(k_{EX}\tau)\right] \quad \text{(eq.1)}$$

where $\delta\omega$ is the chemical shift difference between two sites, and $F_2$ is the exchangeable proton population; $(1\text{-}F_2)$ is the fraction of bulk water protons, $k_{EX}$ is the exchange rate. O is the inter-echo time independent contribution to $R_2$. Multiple regression analysis of the observed $R_2$ using equation 1 gave the parameters of O, $F_2(\delta\omega)^2$ and $k_{EX}$ (Table 1). The calculated $k_{EX}$ is 22000 $s^{-1}$ in gelatin gel and 35000 $s^{-1}$ in agarose gel. $F_2(\delta\omega^2)$ values increased linearly as a function of field strength over the range of 4.7 to 18.8T in gelatin gel as shown in Figure 3. This model equation is only applicable to fast exchange (i.e. $\delta\omega / k_{EX} << 1$). From the literature, if the chemical shift difference of the gelatin is about 1.5ppm as proposed in the literature [4], the measurement conditions may be intermediate to slow exchange. Further study is necessary to analyze the dynamics of the exchange. The ratios of O in relaxation rate were quite different in two gel systems. In gelatin gel, calculated O is close to zero. This result suggests that dynamic dephasing mechanisms are dominating the transverse relaxation in the gelatin gel. On the contrary, O for agarose gel is approximately half of $R_2$, suggesting that the classical dipolar mechanism is dominating in the relaxation in agarose gel.

---

ferritin iron, human brain, transverse relaxation

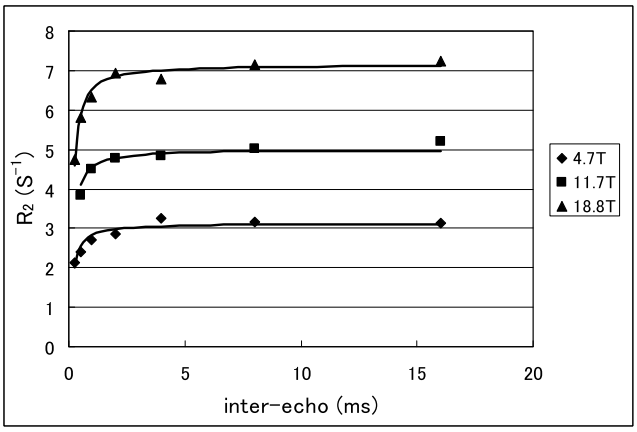


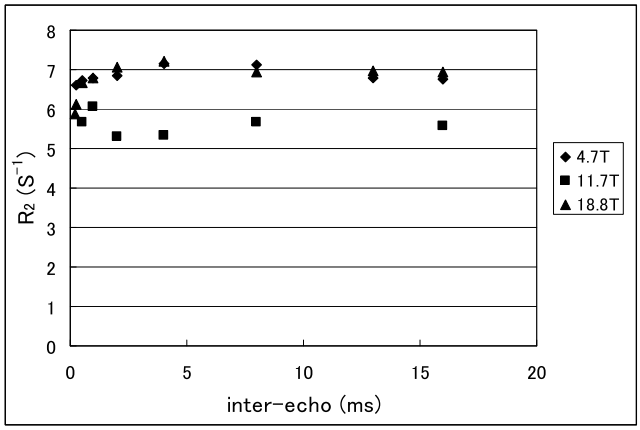


Fig.1 (left) Variation of the $R_2$ as a function of intet-echo time for gelatine gel. Equation (1) was fitted to the data.

Fig.2 (right) Variation of the $R_2$ as a function of intet-echo time for agarose gel.

Table 1. Parameters determined from Eq. (1) for water protons of gelatine and agarose gel at 4.7T, 11.7T and 11.8T

| | O | $F_2(\delta\omega^2)$ at 4.7T | $F_2(\delta\omega^2)$ at 11.7T | $F_2(\delta\omega^2)$ at 18.8T | $k_{EX}$ |
|---|---|---|---|---|---|
| geratin | 0.0 | 69.0 | 110.3 | 157.9 | 22000 |
| agarose | 3.0 | 143.2 | 140.0 | 141.9 | 35000 |

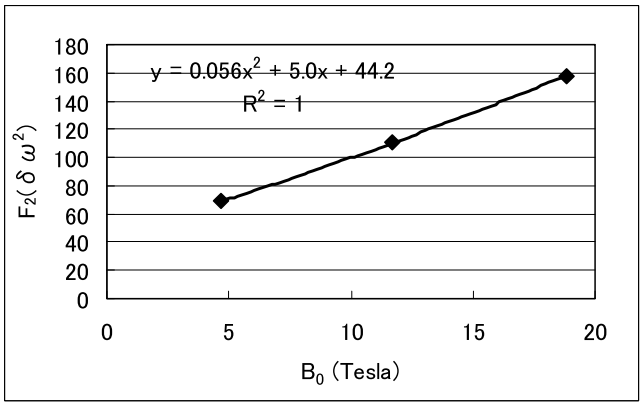


Fig.3 $B_0$ dependence of the parameter of $F_2(\delta\omega)^2$ in gelatin gel.

References

[1] F. Mitsumori, H. Watanabe, N. Takaya, Magn. Reson. Med., Vol.62, 1326-1330 (2009).
[2] N.Takaya, H. Watanabe, F.Mitsumori, The 49th Annual Meeting of The NMR Society of JAPAN. 402-403 (2010)
[3] Luz Z, Meiboom S. J. Chem. Phys. 39: 366-3701(1963).
[4] A. Traore, L. Foucat, J.-P. Renou Eur. Biophys J Vol.29 159-164 (2000)

# P-132 Y

# Application of Statistical Correlation Method for Understanding Complex Gut Ecosystem

Shinji Fukuda[1,2], Yumiko Nakanishi[3], Yasuhiro Date[3], Hiroshi Ohno[1,2], Jun Kikuchi[2,3]
[1]RIKEN Research Center for Allergy and Immunology,
[2]Graduate School of Nanobioscience, Yokohama City University, and
[3]RIKEN Plant Science Center

**[Abstract]**

Recent NMR-based metabolomics studies have contributed to know how intestinal metabolites from host and microbial cells play a key role for maintaining physiological homeostasis of our body. In order to understand metabolic dynamics in the host-microbe symbiotic ecosystem further, we developed novel data mining methods based on statistical calculation of metabolites from digitized NMR spectra, gene expression and microbial community data. We will show how these methods will extend from model bacteria and mouse system to understand the homeostasis and fluctuation in our complex gut ecosystem.

**[Introduction]**

Metabolomics is using analytical techniques such as NMR together with information technology to elucidate bird-eye viewing for metabolism. The byproducts of metabolism, known as metabolites, are produced in biological samples such as various organs, urine, saliva, blood plasma, and intestinal contents. Recent NMR-based metabolomics succeeded to show these metabolite profiles as produced in biological samples and finds out various biomarkers expressing specific metabolic phenotypes [1, 2]. Metabolic phenotypes are the products of interactions among a variety of factors such as diet, other lifestyle/environment, gut microbiome, and genotype [3]. Analyzing metabolites in our body using various spectroscopic methods provides information on the metabolic phenotype of individuals or populations, information that can be applied to personalized medicine or public healthcare.

The symbiotic gut microbes exert a strong influence on the metabolic phenotype of the mammalian host and participates in extensive microbial–mammalian co-metabolism. These symbiotic microbes form a highly complex microbial community in our gut and they have a profound influence on human physiology, immunology, and nutrition. On the other hand, imbalance in the composition of microbes could be a risk factor in human disorders including inflammatory bowel disease, metabolic syndrome, autoimmune disease, and colonic carcinogenesis. However, the molecular mechanisms of symbiotic microbes which exert several physiological effects on human health and diseases through host-bacterial crosstalk remain obscure.

In order to understand the role of symbiotic microbes for maintaining symbiotic gut ecosystem, we firstly established the NMR-based metabolomics approach combined with various statistical correlation methods (Fig. 1)[4-8]. We herein show that the effectiveness of these methods on understanding the complex gut ecosystem.

**Key words:** Multivariate analysis, NMR-based metabolomics, Symbiotic microbes

**[Materials and Methods]**

Development of Real-Time Metabolotyping (RT-MT: Fig.1 right): NMR spectra were recorded on a 500.03 MHz NMR spectrometer at 310 K during bacterial growth anaerobically in NMR tube. For 1D *in vivo* $^{1}$H-NMR spectra were observed every 5 minutes and residual water signals were suppressed by watergate pulse sequence with 1.2 second repetitive time. 2D $^{13}$C-HSQC spectra were measured every 8 minutes according to our previous method (4). For $^{1}$H-NMR profiling, 1D $^{1}$H-NMR data were reduced by subdividing spectra into sequential 0.03 ppm designated regions between $^{1}$H chemical shifts of 0.5 to 9.0 ppm. For 2D $^{13}$C-HSQC profiling, 2D $^{13}$C-HSQC spectra were reduced by subdividing spectra into sequential bins of 0.3 ppm in the f1 direction and 0.03 ppm in f2 designated regions between $^{1}$H chemical shifts of 0.5 to 9.0 and $^{13}$C chemical shifts of 40 to 90, respectively. After exclusion of water resonance from 1D and 2D profiling data, each region was integrated and normalized relative to DSS intensity as an internal standard. All bins were analyzed by principal component analysis (PCA) with the R software and plotted using GraphR. Loading plot analysis revealed the contribution of bins to the PCA scores and 2D spectral assignments were performed using SpinAssign software.

Statistical correlation method for understanding microbes-metabolite interaction (Fig.1 bottom): Microbial composition was analyzed by PCR-based denaturing gradient gel electrophoresis (DGGE) method (6). The DGGE band signals were calculated using Quantity One software. The signal intensities and band position in each lane were divided into a spectrum consisting of 100 variables. A two-dimensional correlation map was calculated as a symmetric matrix using Pearson's product-moment correlation coefficient in which an element at position ($i$, $j$) is defined as a correlation coefficient between the $i$-th and $j$-th positions in a set of two dimensional spectra of assigned metabolites and DGGE gel bands of identified bacteria. A more positive

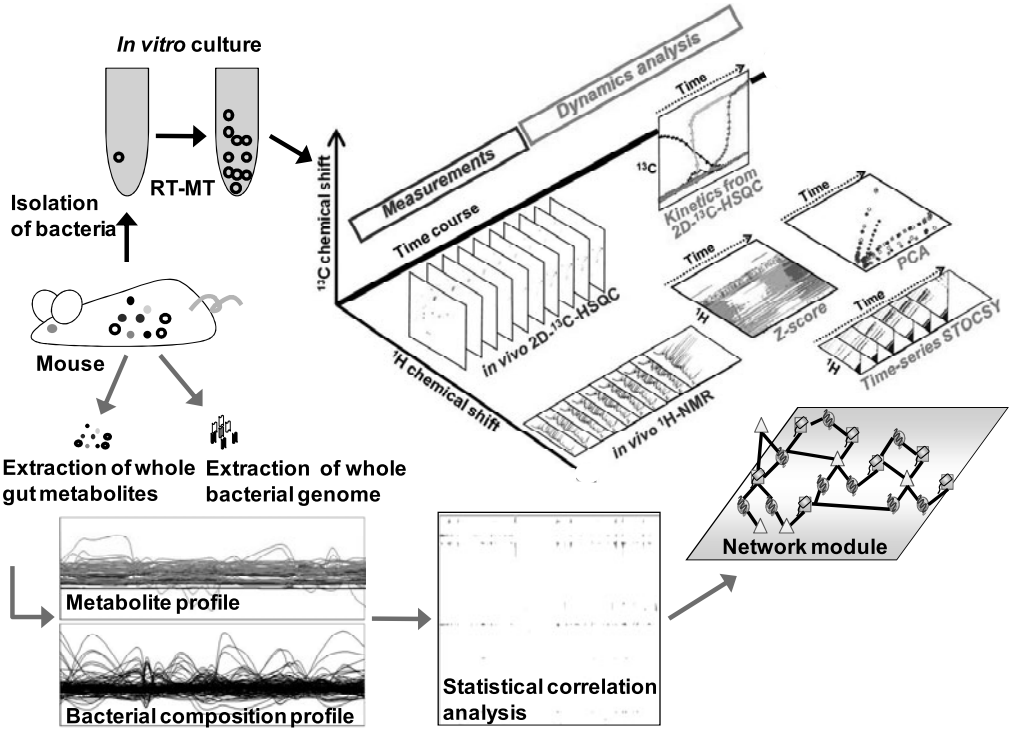


**Fig. 1.** Schematic overview of our application of NMR-based metabolomics with statistical correlation method for understanding complex gut ecosystem. Right: In case of isolated microbes, metabolic dynamics is measured by *in vivo* $^{1}$H-NMR and 2D $^{1}$H,$^{13}$C-HSQC with $^{13}$C labeled substrate technique during bacterial growth in an NMR tube at 37ºC. The profiling data are processed and analyzed by several statistical methods, such as Z-score analysis, principal components analysis (PCA), and time series of statistical total correlation spectroscopy (STOCSY). Left to bottom: Network modules in the symbiotic gut ecosystem are developed based on correlative information among gut symbiotic metabolites, bacterial composition and gene expression profile.

(negative) coefficient means the existence of a positive (negative) correlation between the *i*-th peaks and *j*-th bands.

**[Results and Discussion]**

We developed a novel method called real-time metabolotyping (RT-MT), which performs sequential 1D $^{1}$H-NMR profiling and 2D $^{13}$C-HSQC profiling during bacterial growth in an NMR tube (Fig. 1). The profiles were evaluated with such statistical methods as Z-score analysis, PCA, and time series of Statistical TOtal Correlation SpectrocopY (STOCSY). In addition, using 2D $^{13}$C-HSQC with the stable isotope labeling technique, we observed the metabolic kinetics of specific biochemical reactions based on time-dependent 2D kinetic profiles. Using these methods, we clarified the pathway for linolenic acid hydrogenation by a gastrointestinal bacterium, *Butyrivibrio fibrisolvens.* We identified *trans*11, *cis*13 conjugated linoleic acid as the intermediate of linolenic acid hydrogenation by *B. fibrisolvens,* based on the results of $^{13}$C-labeling RT-MT experiments (5). Thus, RT-MT is useful for the characterization of beneficial bacterium that shows potential for use as a health-promoting agent by producing bioactive compounds.

We next examined the bacterial interaction between enterohaemorrhagic *Escherichia coli* O157:H7 (O157) and *Bifidobacterium longum* (BL) as a pathogenic-commensal bacterial model creating a minimum microbial ecosystem *in vitro* using dynamic omics approaches, consisting of improved 2D $^{13}$C-HSQC metabolic profiling, transcriptomic, and proteomic analyses. Our study revealed that the minimum ecosystem was established by bacterial adaptation to the changes in the extracellular environment, primarily by O157, but not by BL (7). Additionally, the relationship between BL and O157 could be partially regarded as that between a producer and a consumer of nutrients, respectively, especially with regard to serine and aspartate metabolism (7). Thus, our 2D $^{13}$C-HSQC based profiling system can provide a new insight into the primary metabolic dynamics in microbial ecosystems.

To understand the host-bacterial crosstalk in the gut *in vivo*, we used gnotobiotic mice associated with certain bifidobacterial strains and a simplified model of lethal infection with O157, together with an integrated 'omics' approach. Our omics approach identified striking difference in

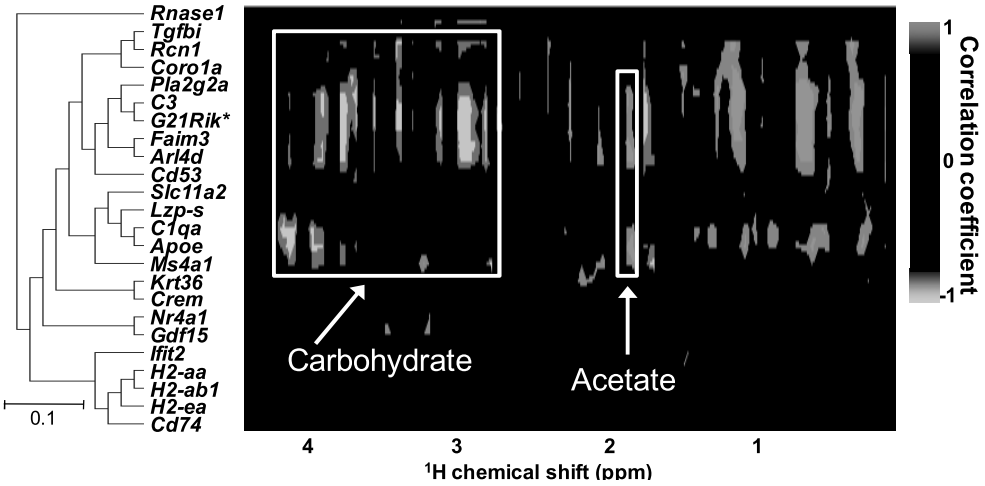


**Fig. 2.** Covariate analysis between gene expression profiles of the colonic epithelium and metabolic profiles of the feces in the bifidobacteria-associated mice. The two-dimensional correlation map was calculated as a matrix in which an element at position (*i*, *j*) is defined as a correlation coefficient (r) between the *i*-th genes and the *j*-th bins in a set of microarray data (24 genes that differed in expression level by more than two-fold between bifidobacteria-associated mice) and $^{1}$H-NMR spectra (n = 3). Covariate analysis of these 24 genes with fecal metabolic difference between bifidobacteria-associated mice indicated a strong correlation of the expression level of some of these genes with the amounts of fecal metabolites, especially amino acids and organic acids (positive correlation: 1.0-2.0 ppm), and carbohydrates (negative correlation: 3.0–4.5 ppm).

the fecal metabolite composition between mice that had been administered the preventive bifidobacterial strains and those that had received the non-preventive bifidobacterial strains. Loading-plot analysis and 2D $^{13}$C-HSQC metabolic profiling identified carbohydrates and acetate, a type of short-chain fatty acids, as the main metabolites that differed between mice associated with the preventive bifidobacterial strains and the non-preventive ones (8). Correlation analysis of the transcriptome of the colonic epithelium and the fecal metabolome of bifidobacteria-associated mice indicated that the acetate could induce anti-inflammatory response in the colonic epithelium, suggesting that mass-produced acetate by the preventive bifidobacteria exerts its action on the colonic epithelium by inducing anti-inflammatory effects, blocking O157 lethal infection (Fig. 2).

To understand the molecular basis of the gut environmental changes including host-bacterial crosstalk followed by highlighting the metabolic pathways of symbiotic microbial community affected by the variation in food ingredient, we developed a novel assessment system for the gut environment based on multiple omics approach. In this study, the changes of metabolic profiles, gut microbial communities, and gene expression profiles caused by the impact of plant-fiber intakes in BALB/c mice were evaluated using NMR-based metabolomics, DGGE, and cDNA library approach. Furthermore, integration of these comprehensive data based on co-correlation analyses, we achieved the prediction of integrated metabolic networks in the changes of gut microbial ecosystems (Fig. 3; unpublished data). Our approach provides a foundation for evaluation of systemic effects of drugs and diet that are of relevance to personal and public health care solutions, and a step for opening up a new window that will clear up metabolic dynamics in the complex microbial community in the gut.

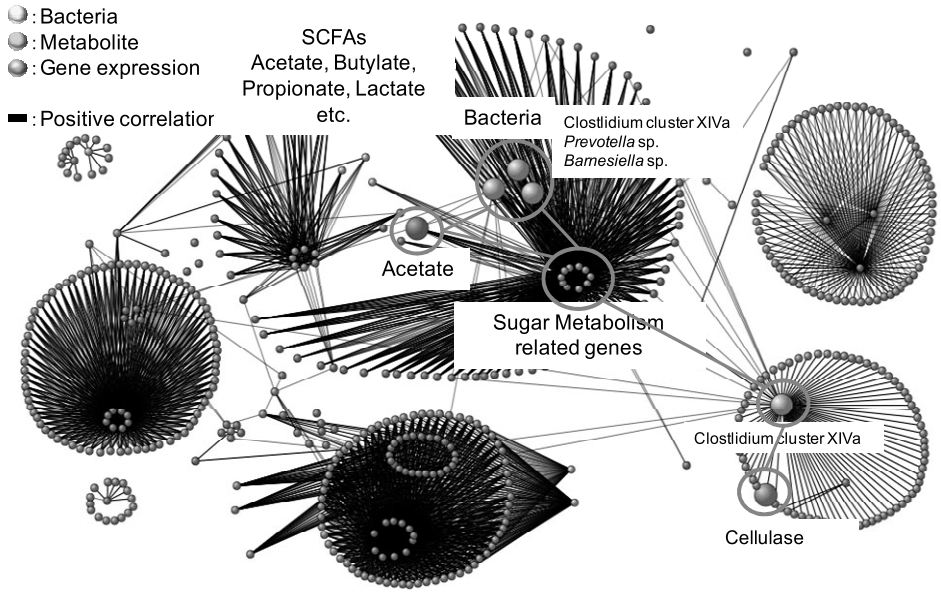


**Fig. 3.** Network module based on co-correlative information of microbial community profile, metabolic profile, and gene expression profile in the symbiotic gut ecosystem. Various metabolites mainly short-chain fatty acids were produced by symbiotic microbes and supplied as nutrients for host cells.

**[References]**


1. Clayton, T. A., Lindon, J. C., Cloarec, O., et al., *Nature*, **440**, 1073-1077 (2006).
2. Holmes, E., Loo, R. L., Stamler, J., et al., *Nature*, **453**, 396-400 (2008).
3. Holmes, E., Wilson, I. D., Nicholson, J. K., et al., *Cell*, **134**, 714-717 (2008).
4. Morita, H., Toh, H., Fukuda, S., et al., *DNA Res.* **15**, 151-161 (2008).
5. Fukuda, S., Nakanishi, Y., Chikayama, E., et al., *PLoS ONE* **4**, e4893 (2009).
6. Date, Y., Nakanishi, Y., Fukuda, S., et al., *J. Biosci. Bioeng.* **110**, 87-93 (2010).
7. Nakanishi, Y., Fukuda, S., Chikayama, E., et al., *J. Proteome Res.* **10**, 824-836 (2011).
8. Fukuda, S., Toh, H., Hase, K., et al., *Nature* **469**, 543-547 (2011).

# P-133 Medical Applications of Metabolomics by $^{1}$H-NMR IV Chiral Separation of Lactate in Renal Dialysate

Seizo Takahashi[1], Ichiro Ando[1], Yutaka Imai1[1],
Kazuhisa Takeuchi[1,2], and Masako Fujiwara[1]
1 Grad. Sch. Pharm. Sci., Tohoku Univ,
2 Koujinnkai Clinic CKD Cnt.

## Abstract:

Spectroscopic separation of D-lactate from abundant L-lactate in the renal dialysates was tried using a chiral active shift reagent together with the enzymatic assay. Aqueous D,L-lactate solution was clearly separated above pH 9.5, however D-lactate was not found in the renal dialysate. It is either due to the masking effect of shift activity by co-existing organic acids or the under-detectable concentration of D-lactate in the dialysate.

## Introduction

Clonic kidney disease (CKD) is a familiar disease that occurs quite often accompanied by blood high pressure, diabetes, dyslipidemia, etc., leading to quite a few circulatory complexes. However, it is still difficult to predict how far their symptoms will develop because of the lack of reliable biomarkers. The metabolome profiling method is a promising approach to find such a set of biomarkers of CKD.

NMR is advantageous for metabonomics studies over other methods, especially against the wastewater during hemodialysis as well as biofluids such as blood serum, urine and saliva. In the dialysate of CKD subjects, the amount of lactate, formate, creatine and other amino acids turned out vary their concentration during the dialysis in a complicated way. For example, a typical change of the lactate concentration is as follows; it decreases first for 30 min then starts to increase and gets maximum about 2 hr later followed by a slow decrease. On the other hand, creatine decreases continuously. Since the amount of small molecules in the blood serum and dialysate makes a parallel change, the result suggests the feedback biosystem is more complex than expected. It is now know the presence of the small amount of D-amino acids in human. However, it is not known for D-lactate in human to our knowledge. The presence of D-lactate implies the activation of methylglyoxal bypass system, and may happen in CKD patients. Thus, we have planned to detect D-lactate in dialysate of CKD subjects.

Keywords: D-Lactate, renal dialysate, chiral shift reagent

## Method

1. Enzymatic Assay

D-lactate and L-lactate assay kit was obtained from Megazyme International Ireland Ltd. through local vender. The principle of the kit is as follows; D-lactate is first oxidized to pyruvate in the presence of nicotineamide-adenine dinucleotide ($NAD^+$), catalyzed by D-lactate dehydrogenase (D-LDH)

(1) D-Lactate + $NAD^+$ $\overset{D-LDH}{\rightleftharpoons}$ Pyruvate + NADH + $H^+$

Then the pyruvate is converted to D-alanine and 2-oxoglutarate in the presence of a large excess of D-glutamate, catalyzed by D-glutamate-pyruvate transaminase (D-GPT).

(2) Pyruvate + D-glutamate $\overset{D=DPT}{\rightleftharpoons}$ D-alanine + 2-oxoglutarate

L-lactate is assayed after reactions (1) and (2) adding L-LDH. The concentration of lactate was calculated from the absorbance at 340nm from NADH.

2. NMR measurement

Chiral shift reagent Sodium [(R)-1,2-Diaminopropane-N,N,N',N'-tetraaceto]-samarium(III) Hydrate was obtained from Tokyo Kasei. Other organic compounds were obtained from Wako. The shift reagent was dissolved ca. 3mg in the sample such as the mixture of 0.52mL of dialysate and 0.02mL of $D_2O$. After adjusted pH to ca. 10 by NaOH and $Na_2CO_3$, the sample was transferred to 5mm standard Shigemi tube. $^1$H-NMR was measured by JEOL GX-600 equipped with Narolac $^1$H-selective probe. The1000 transients of 65K data points were collected with 10 ppm spectral width at room temperature. A program was written by MATLAB for data analysis.

## Results and Discussion

1. Enzymatic assay exhibited the concentration of D-lactate is scarcely over the noise level even for the freeze dried dialysate. The estimated concentration of L-lactate was instable over sample to sample, although the model solution exhibited precisely as predicted. The result suggests that the dialysate contains an inhibitor, most likely the oxidizing contamination, of LDH reaction. Thus, we were unable to verify the presence of D-lactate by the enzymatic reaction.
2. NMR spectral separation of D-lactare from L-lactate was found feasible on model solution of D/L-lactate at pH>9.0. However, it was not detectable of D-lactate under the same condition in the dialysate. NMR results revealed that the dialysate contains something to inhibit the complex formation of shift reagent to lactate. It is certain at least that the amount of D-lactate is less than 10% of L-lactate.

# P-134 An effective assessment of simvastatin-induced toxicity with NMR-based metabonomics approach

Sunmi Kang[1,a], Hye-ji Yang[1,a], Myung-Joo Choi[2,a], He Wen[1,a], Hyuk Nam Kwon[1], Kyung Hee Jung[2], Sang-Won Hong[2], Joon Mee Kim[3], Soon-Sun Hong[2,*], Sunghyouk Park[1,*]

[1]Department of Biochemistry, [2]Department of Biomedical Sciences, [3]Department of Pathology, Inha University Hospital and Center for Advanced Medical Education by BK21 project, College of Medicine, Inha University, Shinheung-dong 3ga, Chung-gu, Incheon, Korea, 400-712

Simvastatin, which is used to control elevated cholesterol levels, is one of the most widely prescribed drugs. However, a daily excessive dose can induce drug-toxicity, especially in muscle and liver. Current markers for toxicity reflect mostly the late stages of tissue damage; thus, more efficient methods of toxicity evaluation are desired.

As a new way to evaluate toxicity, we performed NMR-based metabonomics analysis of urine samples collected from Female Wistar rats. Compared to conventional markers, such as AST, ALT, and CK, the urine metabolic profile provided clearer distinction between the pre- and post-treatment groups treated with toxic levels of simvastatin. Through multivariate statistical analysis, we identified marker metabolites associated with the toxicity. Importantly, we observed that the treatment group could be further categorized into two subgroups based on the NMR profiles: weak toxicity (WT) and high toxicity (HT). The distinction between these two groups was confirmed by the enzyme values and histopathological exams. Time-dependent studies showed that the toxicity at 10 days could be reliably predicted from the metabolic profiles at 6 days.

This metabonomics approach may provide a non-invasive and effective way to evaluate the simvastatin-induced toxicity in a manner that can complement current measures. The approach is expected to find broader application in other drug-induced toxicity assessments.

Simvastatin, Drug-toxicity, NMR-based metabonomics

# P-136 Development of interferogram extrapolation method for NMR experiments that requires accurate peak height

Takumi Ueda[1], Masahiko Matsumoto[1], and Ichio Shimada[1, 2]
[1]Graduate School of Pharmaceutical Sciences. the University. of Tokyo, and [2]BIRC, AIST

**Introduction**

In NMR analyses of membrane proteins or proteins in living cells, which are labile and low concentration, high resolution multidimensional NMR spectra must be acquired with high sensitivity in short time. In multidimensional NMR experiments for the quantitative analyses of structures and dynamics, such as transferred cross-saturation (TCS), NOESY, and relaxation analyses, particularly high sensitivity and accurate peak height are required.

However, acquisition of massive data with large evolution time, in which signal intensities are severely diminished, is required to increase the resolution in multidimensional NMR. Therefore, high resolution usually cannot along with short measurement time and high sensitivity. Although this dilemma can be partly solved by applying linear prediction (LP) for the extrapolation of the data points with large evolution time, the number of the data points extrapolated by LP usually cannot exceed the actual data points, due to signal distortion.

Prior to recording multidimensional NMR, preliminary spectra, such as $^{1}$H-$^{15}$N HSQC, are usually recorded, to optimize the measurement condition. Although such "guide spectra" retain useful information about the resonance frequency and the relaxation rate of each signal, they have seldom been utilized for the data processing. Here, we aimed to develop a multidimensional NMR processing method that utilizes such information on the guide spectra and enables us to obtain high resolution spectra with high sensitivity and accurate peak height in short measurement time.

**Theory**

Interferograms in the multidimensional NMR data with correct phase, F(t), can be represented as a linear combination of $k$ signals, in which $i$th signal has intensity $x_i$, oscillates at frequency $\omega_i$, and decays with relaxation rate $R_i$:

$$\mathrm{F(t)} = \sum_{i=1}^{k} \mathrm{x_i} \exp(-R_i + i\omega_i)t$$

Inputting $R_i$ and $\omega_i$ values of the guide spectra and the actually recoded F(t) values results in simultaneous equations with $k$ unknown values $x_1 ... x_k$. In the previously reported ANAFOR and TIGER methods, the optimal solution of the equations are calculated by least-squares algorithm, and the data points with large evolution time are calculated by inputting the solution to the above equation.

However, it is practically difficult to measure the transverse relaxation rates of labile and/or low concentration samples. Our preliminary calculation revealed that the ratios of the peak heights between two spectra, which are usually used in quantitative NMR, are insensitive to the mismatches of the transverse relaxation rates. Therefore, we input constant relaxation rates in $R_i$.

---

cross-saturation, HSQC, relaxation

## Results

### Evaluation of the applicability of the developed method by simulation

We performed simulations of the developed method, under the experimental parameters typical in the $^{1}H$-$^{15}N$ HSQC analyses of proteins. Fig.1A represents the processed interferogram and spectrum of a single synthetic signal with noise. The interferogram was properly extrapolated even in the presence of noise, and there is little artifacts in the spectra.

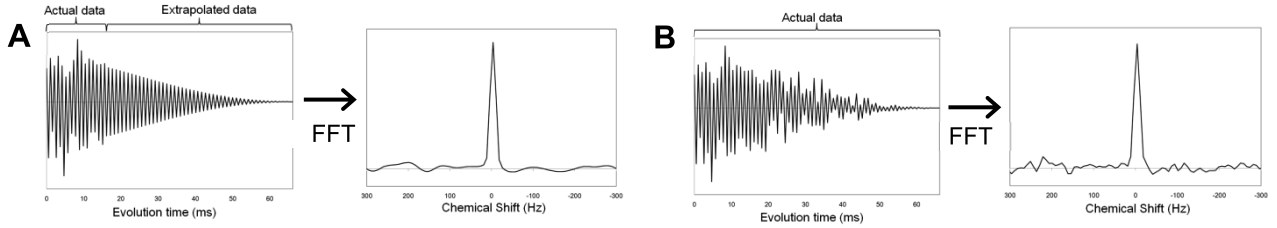


**Fig.1 Interferograms and spectra in the simulation of a single synthetic signal with noise.**
A. 32 actual data points + 96 extrapolated data points, B. 128 full actual data points.

We subsequently performed the simulations under the conditions with obstacles that frequently appear in practical biomolecular spectra. Our simulation revealed that peak height ratios between two spectra can be determined with less than 5 % error, from the spectra with the ratio between the actual and extrapolated data points =1:3, even in the presence of an additional signal with 45 Hz chemical shift difference, 6 Hz frequency mismatch between the actual and guide spectra, and four times transverse relaxation rate mismatch.

### Processing the experimentally recorded data

We applied the developed method to the experimentally recorded TROSY-TCS spectra of [ul-$^{2}H$,$^{15}N$] spinach plastocyanin (99 residues) and non-labeled photosystem I. The processing of each spectrum was finished within one minute in standard PCs. Under the condition with the ratio between the experimentally recorded and extrapolated data points=1:3, the peak height ratio error was less than 0.1, and the residues with peak height reduction ratio > 0.4 were the same as those in the full experimentally recorded data (Fig.2).

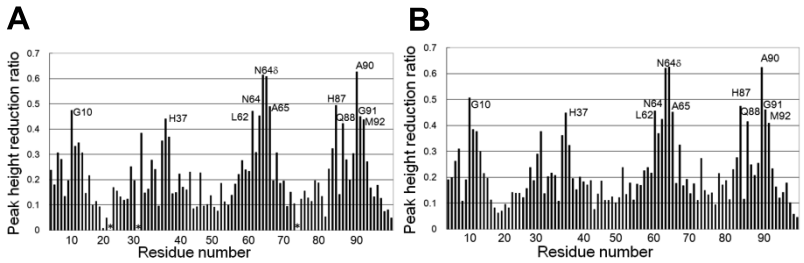


**Fig.2 Plots of the peak height reduction ratios in the TCS experiments of spinach plastocyanin with photosystem I.** A. 16 experimentally recorded data points + 48 extrapolated data points, B. 64 full experimentally recorded data points.

## Discussion

The developed method enables us to halve the measurement time of the LP-utilizing quantitative NMR, with little sensitivity loss or appearance of artifact. This method can also be utilized to improve the sensitivity, without increasing the measurement time. The calculation is computationally simple, thus it does not require expensive servers or softwares. Therefore, this method can readily accelerate various multidimensional NMR analyses that require accurate peak height ratios.

# P-137 New server systems based on virtual computing for the database BMRB and MagRO-Tools for NMR analysis.

Naohiro Kobayashi[1], Takeshi Iwata[1], Yoko Harano[1], Chojiro Kojima[1], Haruki Nakamura[1] and Toshimichi Fujiwara[1]
[1]Institute for Protein Research, Osaka University

ABSTRACT
We have been working on development of the systems and related tools of the database BMRB for NMR experimental data studies on the biological macromolecules in corporation with Wisconsin-Madison University. We have created BESS and MagRO-Tools which can be used for highly automated NMR analysis and assistance to deposit NMR data to BMRB. As the new project supported by NBDC has started at this April, we have been reconstructing our deposition and annotation systems and related tools on new server systems based on virtual computing. We are going to show our recent activities and applications for our client tools and servers in the presentation.

**1. Introduction**

The molecular systems addressed in recent biomolecular NMR studies tend to be more complex, including oligomeric proteins, ligand binding studies, tandemly linked protein domains and so on. Together with the complicated nature of NMR data, the management of NMR data in a local database and the translation of these data to the public database are still tedious tasks.
The BioMagResBank (BMRB) is the standard public database for NMR data of biomolecules, which has grown into a large repository, embracing more than 7,200 released entries for chemical shifts at present (Sept, 2011). As the chemical shift data deposition has been mandatory when NMR structure coordinates are submitted to the PDB since December 2010, more systematic and integrated suite of the programs for NMR data analysis have been strongly desired.

**2. Development of Xen servers for virtual computing**

We have been currently developing new server/client systems based on virtual machine technology called Xen. In the system, a series of virtual machines are working as "virtual servers" including the automated deposition servers, ADIT-NMR and SMSDep and the public database server, BMRB-Web. As shown in the Fig. 1, the system has high robustness against failure due to unforeseen problems happen on the hardware.

**3. MagRO-Tools for analysis of NMR data**

Recently we have developed new NMR data analysis tools MagRO-Tools, including MagRO-Assign for highly automated assignment of NMR signals, MagRO-Graph for making coherence transfer graph of NMR spectrum, MagMol for visualisation and validation of NMR structure and data and MagRO-BMRB for assistance of deposition of assigned chemical shift data to BMRB. They systematically work with the data structure according to the ontology files created by MagRO-Core that we released in the last fiscal year. The MagRO-Core has been implemented in the NMR spectrum viewer, NMRView and Sparky as the user can manage the complicated system for NMR studies (see Fig. 2). We are also developing server systems which may work with the MagRO-Tools as clients which may help the user to avoid the installation works of the programs and as well as to access information related to the target samples from the public database, such as PDB and BMRB.

Database, BMRB, Analysis

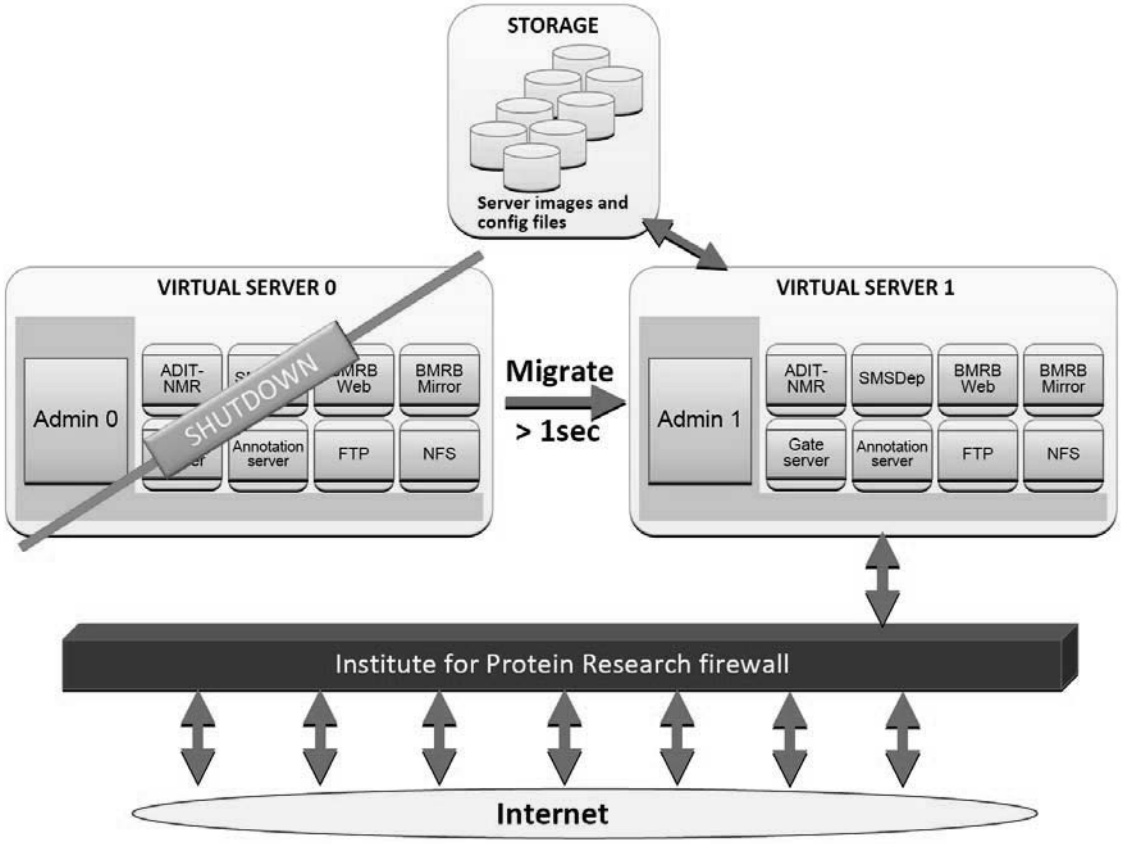


Fig. 1. A conceptual representation of the fail-over live migration system built in the virtual machines. When one of the servers has been shutdown, all virtual machines can migrate to the other available server immediately (within 1 sec).

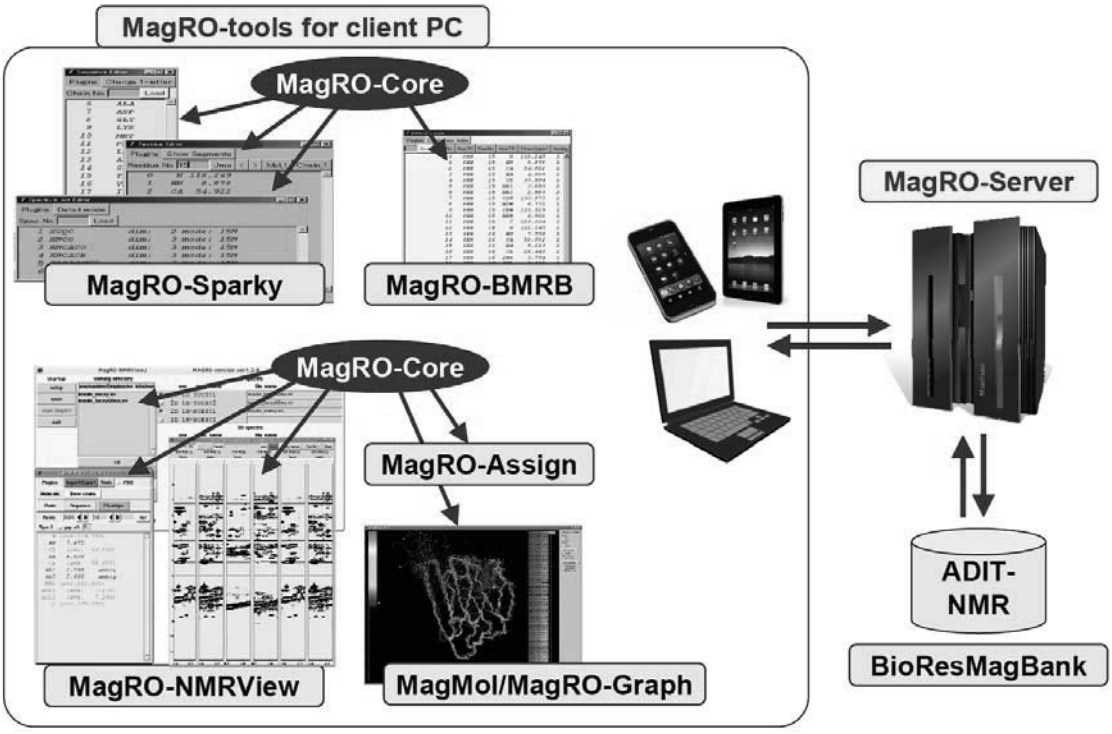


Fig. 2. MagRO-Tools controlled by the internal database manager magRO-Core.

# P-138 Software tool for sequence-specific resonance assignment of proteins using the lanthanide probe method

Masashi Yokochi[1], Tomohide Saio[1] and Fuyuhiko Inagaki[1]
[1]Faculty of Advanced Life Science, Hokkaido University

Abstract
Pseudocontact shifts (PCSs) induced by paramagnetic lanthanide ions bound to proteins provide a rich source of long-range restraints for structural study of proteins. Here, we present a program simultaneously to determine the resonance assignment, the Δχ tensor and the position of the lanthanide ion based on the PCS data. The program requires the protein structure and PCS data. Examples are demonstrated for p62 PB1 domain (100 a.a.) and E. coli MurD D1D2 domain (302 a.a.).

## Introduction

PCSs can be interpreted directly in association with Δχ tensor parameters: $\Delta\chi_{ax}$ and $\Delta\chi_{rh}$ and positions of the observed nuclei relative to the lanthanide ion (Eq. 1) where r is distance from the lanthanide ion and θ, φ define angles of polar coordinates in principal axis of Δχ tensor.

$$\delta^{PCS} = \frac{1}{12\pi r^3}\left[\Delta\chi_{ax}\left(3cos^2\theta - 1\right) + \frac{2}{3}\Delta\chi_{rh}\left(sin^2\theta cos2\varphi\right)\right] \quad \text{(Eq. 1)}$$

If both protein structure and resonance assignment are available, PCSs can be used for structure determination of protein-protein complexes and protein-ligand complexes. If both protein structure and PCS data are available, the sequence-specific resonance assignment based on the structure is feasible. The application for sequence-specific resonance assignment based on PCS data has been made for metalloproteins but hasn't been applied to intrinsically diamagnetic proteins because of difficulty to determine the position of the metal ion fixed by the Lanthanide Binding Tag (LBT). We present here a practical approach and a software tool simultaneously to determine the sequence-specific resonance assignment, the position of the lanthanide ion and Δχ tensor using amino acid selectively labeled protein attached by either Two-point anchored LBT or Caged Lanthanide NMR Probe (CLaNP). In order to demonstrate the structure-based assignment, we tested two cases; (i) p62 PB1 (3-100) utilizing Two-point anchored LBT and (ii) MurD D1D2 (1-302) utilizing CLaNP-5.

## Methods

1. Sample preparations

Program requires PCS and NOE data (optional) obtained by the residue-specific labeled and deuterium labeled sample, respectively. We prepared several samples of p62 PB1 and MurD D1D2 as follows.

(i) $^{15}$N-Arg-, $^{15}$N-Phe- or $^{15}$N-Leu labeled p62 PB1 C42S/D67A/D69A containing LBT

Pseudocontact Shift(PCS), Residual Anisotropy Chemical Shift(RACS), Assignment

was prepared according to the procedure reported previously (Ref. 1), and used for PCS measurement. LBT was attached to p62 PB1 via N-terminal fusion point and disulfide bond mediated by C26 in oxidized condition.

(ii) $^{15}$N-Leu-, $^{15}$N-Val-, $^{15}$N-Ile- or $^{15}$N-Met-labeled MurD D1D2 (1-302) containing CLaNP-5 was prepared. We designed three constructs of MurD D1D2 that have cysteine mutations at different regions: T54C/S56C (#1), M145C/D148C (#2), and E260C/K262C (#3). The CLaNP-5 tag was introduced to the protein according to the previous procedure (Ref. 4).

2. Program features

PCS signals were identified manually using NMR spectra viewer application in the Olivia program. Then, the PCS analysis program, pcs2assign, solves assignment to minimize total differences between experimental PCS and back-calculated PCS+RACS values, $E^{pcs}$ (Eq. 2), using Hungarian method on grid points changing the $\Delta\chi$ tensor parameters roughly at first and finely at last. RACS is derived from incomplete averaging of CSA tensor of observed nuclei in weakly aligned condition caused by magnetic susceptibility of paramagnetic ion. k and n in Eq. 2 are nuclide and observed nuclei, respectively. $\Delta_k$ is error tolerance for nuclide k.

$$E^{PCS} = \sum_{k,n}\left(\frac{\delta_{calc,k,n}^{PCS+RACS} - \delta_{exp,k,n}^{PCS}}{\Delta_k}\right)^2 \quad \text{(Eq. 2)}$$

Then, the assignments are determined using the best $\Delta\chi$ tensor parameters obtained by the grid search and the $\Delta\chi$ tensor parameters are subsequently determined by least square method. Finally, both the assignments and the $\Delta\chi$ tensor parameters are evaluated by Monte Carlo simulation and 3D NOESY spectra.

Results

1. Assignment of backbone amide group of p62 PB1 (DR) domain

PCSs of 24 residues were measured and identified (Arg:9, Phe:6, Leu:9) using various lanthanide ions ($Tm^{3+}$, $Er^{3+}$, $Dy^{3+}$, $Tb^{3+}$). To find $\Delta\chi$ tensor parameters without knowing resonance assignments, We must conquer high dimension numbers of the $\Delta\chi$ tensor parameters, 3 + 5n, where 3 for Cartesian coordinates (x,y,z), 5 for $\Delta\chi$ tensor parameters ($\Delta\chi_{ax}$, $\Delta\chi_{rh}$, Euler angles ($\alpha$,$\beta$,$\gamma$)) for each metal ion and n represents total number of lanthanide ions. First, we introduced unified principal coordinate for all lanthanide ions due to small difference in different lanthanide ions. The principal components of $\Delta\chi$ tensor, $\Delta\chi_{ax}$ and $\Delta\chi_{rh}$ are set to typical values referring to previous study about metalloprotein of Calbindin (Ref. 2, 3) so that we can reduce dimension numbers to 3 + 3 at initial step of grid search. In the latter steps, we introduced z-axis unified coordinate that allows variations in orientation of x-y plane for each lanthanide ions. Details and results of grid search are summarized in Table 1.

All PCS signals were assigned correctly using the grid search protocol. $\Delta\chi$ tensor was subsequently determined by refinement step using Monte Carlo simulation. The result is comparable with the previous work (Table 2, 3 and Figure 1). Overall assignment consistency is 99.96% through the simulations.

**Table 1** Search strategy for determination of Δχ tensor parameters and resonance assignment

| | Position Å | Tensor Axes ° | $\Delta\chi_{ax}$, $\Delta\chi_{rh}$ | $E^{pcs}$ | Assignment % |
|---|---|---|---|---|---|
| Step 1 | 3 (full) | 10 *u | Default | (6.574) | 67 |
| Step 2 | 0, ±2, ±4 | 0, ±5 *u | 0, -5, -10 | (3,897) | 71 |
| Step 3 | 0, ±1, ±2 | 0, ±10 *z | Fix | (1.954) | 92 |
| Step 4 | 0, ±0.5, ±1 | 0, ±5 *z | Fix | 0.677 | 100 |
| Step 5 | 0, ±0.25, ±0.5 | 0, ±2 *z | Fix | 0.494 | 100 |
| Step 6 | 0, ±0.1, ±0.2 | 0, ±1 *z | Fix | 0.478 | 100 |
| Minimize | Optimize | Optimize | Optimize | 0.165 | 100 |

*u and *z represents unified coordinate and z-axis unified coordinate respectively.

**Table 2** Δχ tensors parameters determined using Arg, Phe and Leu PCS signals (24 residues)

| | $Tb^{3+}$ | $Tm^{3+}$ | Dy3+ | Er3+ |
|---|---|---|---|---|
| $\Delta\chi_{ax}$ | 38.4 (7.1) | -22.2 (4.5) | 27.8 (5.7) | -9.1 (2.2) |
| $\Delta\chi_{rh}$ | 21.7 (3.4) | -17.9 (2.1) | 21.0 (3.8) | -7.8 (1.3) |
| α | 117.9 (3.6) | 110.0 (6.8) | 122.9 (3.7) | 117.1 (5.9) |
| β | 107.3 (2.9) | 110.0 (3.1) | 108.5 (2.7) | 109.4 (3.1) |
| γ | 14.2 (6.2) | 0.6 (5.2) | 36.6 (3.9) | 15.9 (5.3) |

Position of metal ion is x, y, z = 5.55 (0.97), 14.98 (0.68), 14.32 (0.69) where the parenthesis stands for standard error.

**Table 3** Δχ tensors parameters reported in the previous work (64 residues) (Ref. 1)

| | $Tb^{3+}$ | $Tm^{3+}$ | $Dy^{3+}$ | $Er^{3+}$ |
|---|---|---|---|---|
| $\Delta\chi_{ax}$ | 40.8 (1.1) | -27.2 (1.3) | 28.6 (1.5) | -10.4 (0.3) |
| $\Delta\chi_{ax}$ | 20.7 (0.9) | -18.9 (1.0) | 21.7 (1.0) | -9.1 (0.2) |
| α | 119 | 114 | 124 | 114 |
| β | 106 | 107 | 108 | 107 |
| γ | 15 | 2 | 37 | 14 |

Position of metal ion is x, y, z = 5.11, 15.55, 15.16. The parenthesis stands for standard error.

Fig. 1 Estimated metal ion positions of LBT-p62 PB1 (DR) by Monte Carlo simulations

## 2. Assignment of backbone amide group of MurD D1D2 domain

MurD D1D2 is 32.7 kDa molecule and its size is about 60*30*20 Å. PCS is not effective in the case where the distance from a paramagnetic center is beyond 40 Å.

Therefore we prepared multiple paramagnetic centers to cover whole molecule by multiple PCS fields. CLaNP-5 is applied for this purpose (Ref. 4). Three sites on the surface of MurD D1D2 were selected as anchoring points of CLaNP-5 by Cys mutations on T54C/S56C (#1), M145C/D148C (#2), and E260C/K262C (#3) referring to the structure (PDB: 3UAG). Backbone assignment was performed for Ile, Met, Leu and Val residues using PCSs derived from $Yb^{3+}$ and $Tm^{3+}$ ions fixed by CLaNP-5 (Fig. 2).

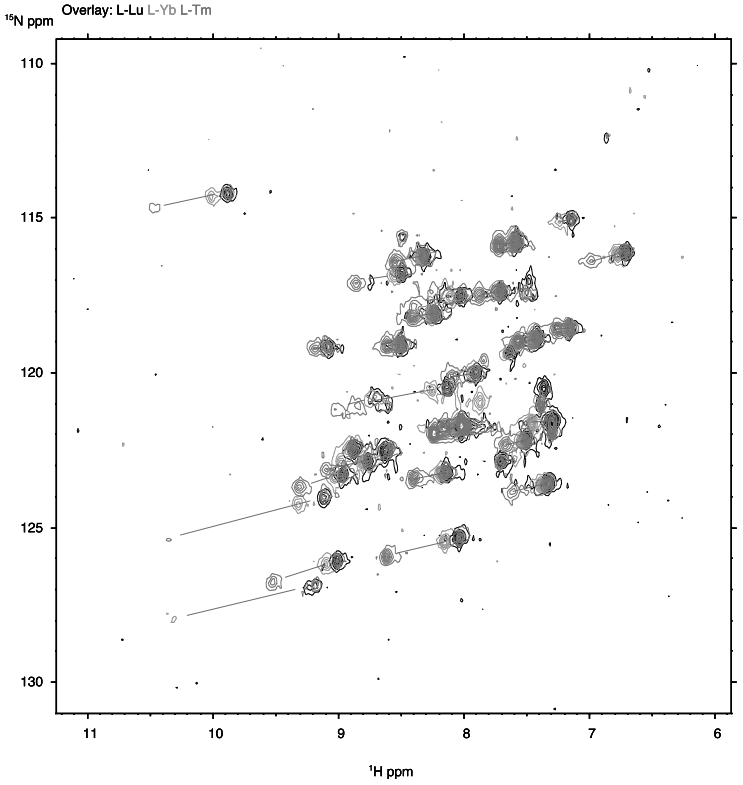


Fig. 2 PCS measurements using $Lu^{3+}$, $Yb^{3+}$ and $Tm^{3+}$ ions about Leu residues of MurD D1D2 T54C/S56C-CLaNP-5

We expanded the search algorithm to support both multiple paramagnetic centers and 3D NOESY spectra and determined 98.8% backbone assignments by considering three paramagnetic centers and 3D NOESY spectra altogether (Table 4).

Table 4 Backbone assignment of MurD D1D2 using multiple paramagnetic centers

| Data set | Assignment % | $E^{pcs}$ |
|---|---|---|
| #1 | 42.2 | 0.043 (#1) |
| #1 and #2 | 96.2 | 0.025 (#1), 0.036 (#2) |
| #1, #2 and #3 | 92.7 | 0.037 (#1), 0.050 (#2), 0.056 (#3) |
| #1, #2, #3 and NOESY | 98.8 | 0.031 (#1), 0.053 (#2), 0.039 (#3) |

References

1 Saio et al., J. Biomol NMR (2010) 46:271-280
2 Pintacuda et al., Acc. Chem. Ref., 2007, 40 (3), 206-212
3 Otting, J. Biomol NMR (2008) 42:1-9
4 Keizers et al., J. Am. Chem. Soc., 2008, 130, 14802-14812

# P-139 Laplace Transformation of FID Signal: A high-precise Pole Estimation Method by Excess High-order ARMA Approximation and Choice of Poles by their Peak Power

Tomoki Nakao[1], Gota Kawai[2], Toshihiro Furukawa[1], and Hajime Kubota[3]
[1]Department of Industrial Engineering, Tokyo Univsity of Science,
[2]Department of Life and Environmental Sciences and
[3]Department of Electrical, Electronic and Computer Engineering,
Chiba Institute of Technology,

**Abstract:**

In molecular structure analysis by NMR, both the resonant frequency and decay factor, in a word, the pole of FID signal is important, and the pole is estimated from the FFT spectrum of the FID signal in FT-NMR method. However, when some peaks overlapping in spectrum domain, it is difficult to estimate the decay factor from peak shape for complicated spectra. In order to overcome the problem above, the pole estimation method by the ARMA model approximation was proposed. However, when FID signal has unevenly-distributed poles, it is difficult to estimate the pole of the FID signal by the method proposed previous. Here we propose a highly accurate pole estimation method by the excessive higher-order ARMA model and choice of pole by peak power to this problem.

**Introduction:**

The resonant frequency and decay factor, which are identical to pole of the signal, are obtained by Laplace Transformation the FID signal. The pole estimation method by the Auto Regressive Moving Average (ARMA) model approximation used as a generation model of the FID signal is proposed based on this idea. From the fact that the FID signal is presented with the linear combination of the exponential decay signal of p piece, the FID signal can be impulse response of ARMA ($p$, $p$-1) model. The pole of the FID signal is obtained from parameter of the model, and p is called the order of FID signal. However, in the conventional method, when the FID signal has unevenly-distributed poles, the error of estimation may happen easily by the influence of the observation noise. This problem can happen even if SN ratio of the signal is very excellent.

In order to overcome the problem above, we propose a highly accurate pole estimation method by the excessive higher-order ARMA model approximation and choice of pole by their peak power. From some numerical examples, when the FID signal has unevenly-distributed poles, the estimation accuracy of the poles can be improved by the estimation model with much larger order than that of the FID signal. Therefore, ARMA ($q$, $q$-1) model is recommended as the poles estimation method, where $q$ is much larger than $p$. This is equivalent to the expression of the observation signal with the linear combination of more exponential decay signals than those of the FID signal. As a result, the poles of the FID signal are included in estimated poles. Therefore, the poles of the FID signal are selected by comparing the peak power of each estimated pole at the end, where we consider the peak power as the power of the exponential decay signal corresponding to each estimated pole. That is, we consider the peak power corresponding to the pole of FID signal is large compared with the other estimated pole.

Laplace Transformation , ARMA model, pole estimation

**Relation between FID signal and ARMA model:**

It is well established that the FID signal can be represented by following

$$h(t) = \sum_{k=1}^{p} c_k \exp(s_k t) \quad , \qquad (1)$$

where $p$ is the number of peak of FID signal, $s_k = -d_k + j2\pi f_k$. $c_k$ is the amplitude, $d_k$ the damping factor, $f_k$ the resonant frequency. $p$ is called order of the FID signal for reasons of expediency. From Eq. (1), the system function of the FID signal given by

$$H(z) = \frac{b_0 + b_1 z^{-1} + \cdots + b_{p-1} z^{-(p-1)}}{1 + a_1 z^{-1} + a_2 z^{-2} + \cdots + a_p z^{-p}} = \frac{b_0 + b_1 z^{-1} + \cdots + b_{p-1} z^{-(p-1)}}{\prod_{k=1}^{p} \{1 - \exp(s_k T_s) z^{-1}\}} \quad , \qquad (2)$$

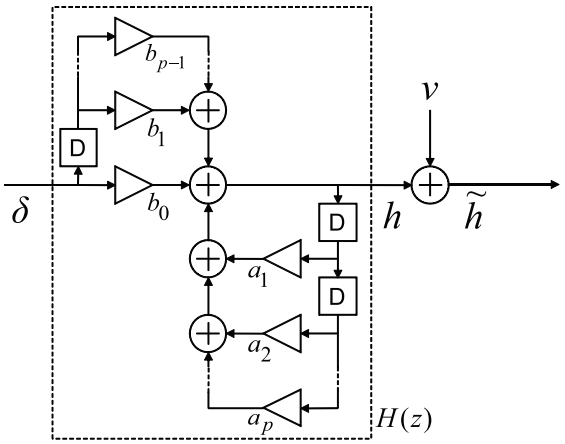


**Fig. 1 The ARMA(p,p-1) model**

Fig. 1 shows the structure of the $H(z)$. $T_s$ is the sampling period, $\boldsymbol{\delta}$ the impulse signal, $\boldsymbol{h}$ the desired signal (FID signal), $\tilde{\boldsymbol{h}}$ the observed signal, $\boldsymbol{v}$ the noise, $a$ the AR coefficient, $b$ the MA coefficient. Therefore, the poles of the FID signal are obtained from AR coefficient. However, when FID signal has unevenly-distributed poles, the error of estimation may happen easily by the influence of the observation noise. This problem can happen even if SN ratio of the signal is very excellent.

**Excess high-order ARMA model approximation and choice of poles by their peak power:**

From some numerical examples, when the FID signal has unevenly-distributed poles, the estimation accuracy of the poles can be improved by the estimation model with much larger order than that of the FID signal. Therefore, ARMA ($q$, $q$-1) model is recommended as the poles estimation method, where q is much larger than p. So, the estimation model is

$$\tilde{H}(z) = \frac{\tilde{b}_0 + \tilde{b}_1 z^{-1} + \cdots + \tilde{b}_{q-1} z^{-(q-1)}}{1 + \tilde{a}_1 z^{-1} + \tilde{a}_2 z^{-2} + \cdots + \tilde{a}_q z^{-q}} \quad , \qquad (3)$$

where $q$ is assumed to be much larger than $p$ ($q \gg p$). And, Eq. 3 is equivalent to the expression of the observation signal with the linear combination of exponential decay signals more than the FID signal.

As a result of estimation by Eq. 3, it is estimated the pole more than the pole of FID signal. It is selecting the pole of FID signal by comparing the peak power corresponding to each estimated pole. That is, we assume the peak power corresponding to the pole of FID signal is large compared with the other estimated pole. Number of selected pole is called select order $\acute{p}$ if $p$ is already-known, it is assumed $\acute{p} = p$. And, if $p$ is unknown, it is detected by visual inspection on spectrum domain.

**Applying to NMR data:**

In this section, the result of applying proposed method to NMR data of uridine is shown. The number of data point is $2^{13}$, the order of proposed model is 400 ($q = 400$), the select order is 40 by visual inspection. Fig. 2 (a) shows the real of FFT spectrum (absorption spectrum) of the FID signal of uridine, where horizontal axis is normalized frequency. Fig. 2 (b) shows the estimated poles (+) of the FID signal of uridine by proposal method, where horizontal axis and vertical axis are resonant frequency and decay factor of estimated pole, respectively. The region indicated by broken box is expanded in Fig. 3, where the band of broken box is called sub band. And, due of space limitations, the maximum of the vertical axis is 0.01.

From Fig. 3, in -0.068Hz and -0.085Hz band around, it is seen that the estimated poles corresponding to each peak on spectrum domain. However, in -0.098Hz band around, not match the number of peaks and estimated poles. Thus, in -0.098Hz band around, the error of estimation has happened. And, the same applies to other than sub band.

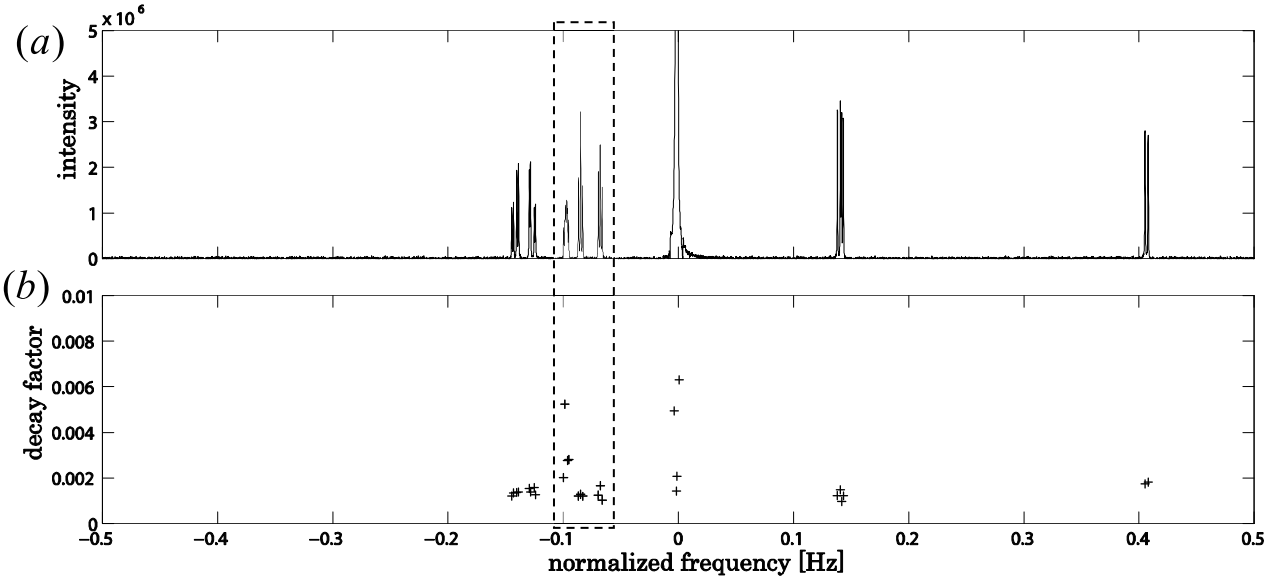


**Fig. 2 The result of analysis of FID signal of uridine (whole band)**

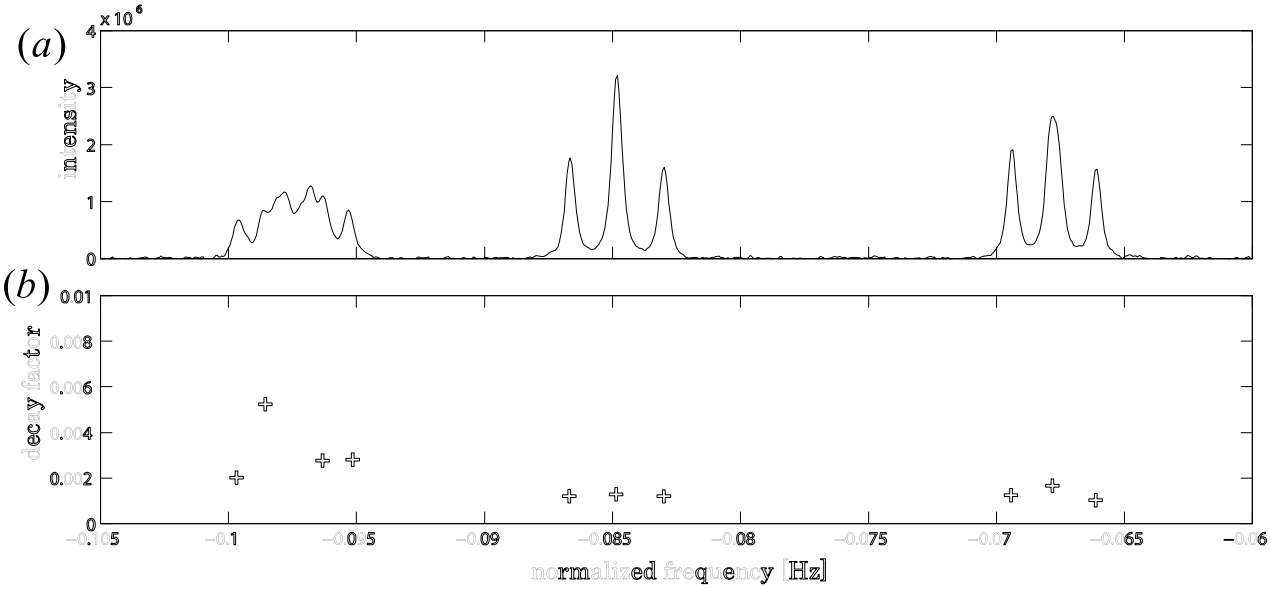


**Fig. 3 The result of analysis of FID signal of uridine (sub band)**

**Compare the absorption spectrum of the FID signal with the estimation signal:**

This section, we compare the estimation signal with the FID signal, where we consider the estimation signal as the output of the ARMA (q,q-1) model with the input being narrow-width pulse. Fig. 4 shows the absorption spectrum of the FID signal and the estimation signal. The region shown in Fig. 4 is the same region with Fig. 3 where the error of estimation happened in the previous section.

From Fig. 4, in -0.098Hz band around, the absorption spectrum of the FID signal is very different from that of the estimation signal. This result is may derived owing to the estimation error of the poles of the FID signal.

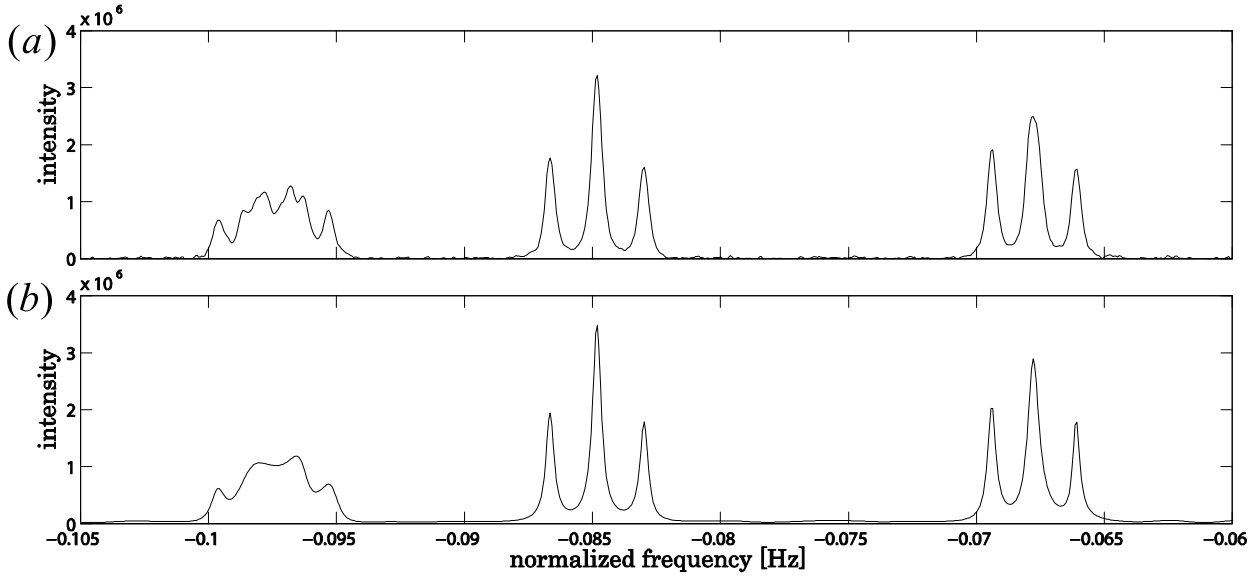


**Fig. 4 The absorption spectrum of the each signal (sub band)**

**Conclusion:**

As a method for estimating the pole of the FID signal, we propose a highly accurate pole estimation method by the excessive higher-order ARMA model approximation and choice of pole by their peak power. The method was applied to the NMR data of uridine, showning that the proposed method is effective for the estimation of the pole of the FID signal. However, it is not sufficient verification regarding the validity of the proposed method. And, in -0.098Hz band around, accuracy of the pole estimation is not enough. It is guested that the main reason for the poles estimation error may be related with unevenly-distributed poles of the FID signal.

**References:**

1) K. Murata and H. Kubota, ‘A precision pole estimation method based on the AR process and an application to the DNA structure analysis IEICE Vol.J91-A No.8 pp.772-781, 2008
2) K. Murata, G. Kawai, T. Furukawa and H. Kubota, ‘A highly precise estimation method for unevenly-distributed poles on NMR by band extraction and its application to NMR spectrum analysis IEICE Vol.J93-A No.7 pp.447-459, 2010

# P-140 Boosting Protein Dynamics Studies Using Quantitative Non-Uniform Sampling NMR Spectroscopy

Yoh Matsuki[1], Tsuyoshi Konuma[2], Toshimichi Fujiwara[1] and Kenji Sugase[2]
[1]Institute for Protein Research, Osaka University, and [2]Bioorganic Research Institute, Suntory Foundation for Life Sciences

## ABSTRACT

We extended the utility of non-uniform sampling (NUS) NMR spectroscopy to a protein dynamics study, where highly accurate spectral quantification is demanded. The use of NUS with quantitative and noise-tolerant SIFT (Spectroscopy by Integration of Frequency and Time domain information) processing produced a 10-fold reduction in measurement time while preserving analytical accuracy. This should significantly broaden the scope of protein dynamics studies.

## INTRODUCTION

NMR spectroscopy is uniquely suited to study protein dynamics over a wide range of time scales. However, most NMR relaxation methods for protein dynamics studies require highly serial, lengthy data collection, limiting their application to short-lived samples. In recent years, the utility of NUS NMR methodologies has been increasingly recognized, but their application has been rare in relaxation measurements where highly accurate spectral quantification is demanded. Recently, we developed a new NUS-processing method, SIFT, which is robust and faithful in reproducing signals. In this work, we further developed SIFT for allowing it to process NUS data recorded without oversampling in the indirect dimension as was required for the previous version. This improvement is crucial for SIFT to be used in accelerating relaxation measurements while preserving full analytical accuracy. We demonstrate that this quantitative NUS processing method enables total 10-fold expedition of the $R_2$ relaxation dispersion measurements. The new version of SIFT should be equally useful for other NMR relaxation measurements.

## MATERIALS AND METHODS

SIFT reinstates missing time-domain samples as much as the information given by "dark" spectral points (regions devoid of any signal) without parameter tweaking for the process. The processing is most accurate when the number of dark spectral points exceeds the number of unmeasured elements in the NUS time domain. In the previous applications of SIFT, dark spectral regions were produced by an oversampling. However, as long as SIFT relies only on the dark information produced by oversampling, the experimental time can never be saved as compared with the experiments conducted without oversampling (Fig 1).

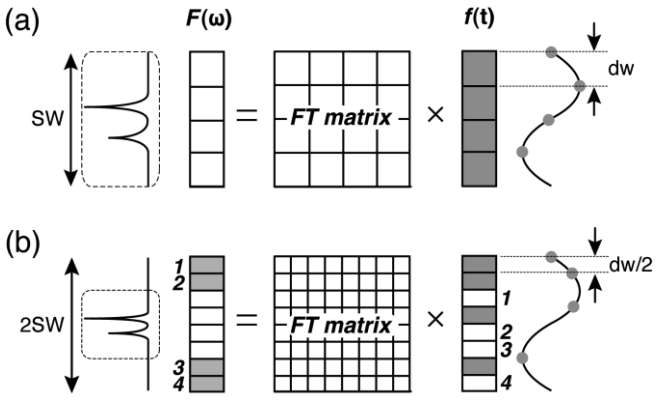


**Fig 1** A cartoon illustrating time- and frequency-domain data, $f(t)$ and $F(\omega)$, paired with the Fourier transform matrix in the cases of Nyquist sampling (a) and twice-oversampling NUS (b). Gray rectangles represent known or measured data points either in the frequency or time-domain.

protein dynamics, non-uniform sampling, quantitative data processing

Oversampled wider bandwidth produces known dark spectral points, but produces also the same number of unknowns in the time domain due to smaller Nyquist grid. Here, we extended the SIFT program so that it can find dark points within a fully native spectrum. A key idea is that in many NMR relaxation experiments, one is interested in accurately measuring the change in peak intensities relative to those in the reference spectrum. Because signal positions are invariant over the serial measurements, one could use all the dark spectral points existing between NMR peaks for SIFTing to accelerate all the subsequent measurements.

## RESULTS AND DISCUSSIONS

We applied the new SIFT protocol to $R_2$ relaxation dispersion measurements for KIX, which is known to undergo a two-state conformational exchange. In the reference spectrum of KIX (Fig 2a), all regions outside the peak positions, specified by rectangles, were treated as dark regions for SIFT processing. For the serial 2D measurements, we used a NUS that randomly distributes 25 $t_1$ samples over 64 Cartesian grids in the time domain. The spectrum before SIFT was highly corrupted with NUS noise (Fig 2b). However, after SIFT, the NUS noise was removed (Fig 2c), and the peak intensities were accurately restored (Fig 2d, middle). The accurate peak intensities measured in the post-SIFT spectra were translated into $R_2$ dispersion profiles resulting in accurate exchange parameters. Two global parameters extracted from the post-SIFT profiles ($k_{ex}$ = 599.72 ± 4.18 $s^{-1}$, $p_B$ = 3.62 ± 0.02%) were in good agreement with the "true" values ($k_{ex}$ = 600.17 ± 4.18 $s^{-1}$, $p_B$ = 3.56 ± 0.02%). The total data acquisition time was compressed to 7.2 h down from 18 h needed on each magnetic field.

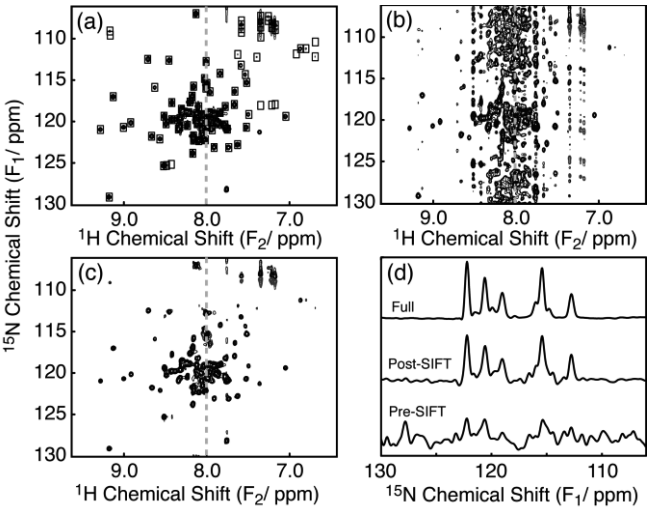


**Fig 2** The reference spectrum of KIX. Fourier transform of fully acquired data (a), and Fourier transform of NUS data before (b) and after (c) SIFT processing. A representative slice indicated by a dashed line in (a), (b), and (c) is shown in (d) for the full (top), post-SIFT (middle), and pre-SIFT (bottom) spectra in the same vertical scale.

The unique robustness of SIFT in processing noisy data should allow for accurate peak intensity measurements in a noisier dataset. Subsequently, we analyzed $R_2$ dispersion data of KIX recorded with only 2 scans per FID instead of 8 scans employed in the above experiments. Despite a factor of 2 deterioration in the S/N ratio, fairly accurate dynamics parameters were obtained after SIFT ($k_{ex}$ = 592.50 ± 21.5 $s^{-1}$, $p_B$ = 3.59 ± 0.09%). The approach yields another factor of 4 acceleration of the measurement, leading to the total measurement time of < 2 h, *i.e.* total 10-fold reduction in measurement time, while minimally affecting the accuracy of the measurement.

## CONCLUSION

We have introduced NUS and new SIFT processing into a protein dynamics study, which represents a novel application of NUS to cases where highly accurate peak quantification is demanded. NUS and SIFT would significantly widen the applicability of NMR-based dynamics studies to more difficult systems with limited sensitivity and stability, enabling these studies to encompass a greater diversity of biological processes than are currently accessible.